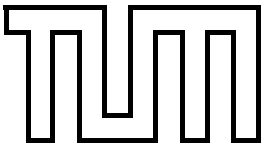

TECHNISCHE UNIVERSITÄT MÜNCHEN

ÉCOLE POLYTECHNIQUE
FÉDÉRALE DE LAUSANNE

Master's Thesis

Computational Science and Engineering
International Master's Program
at the Faculty of Informatics

EFFICIENT SAMPLING FOR ACCELERATED DIFFUSION MAGNETIC RESONANCE IMAGING

Maryna Babayeva

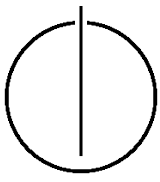

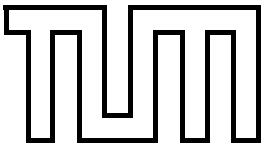

TECHNISCHE UNIVERSITÄT MÜNCHEN

ÉCOLE POLYTECHNIQUE
FÉDÉRALE DE LAUSANNE

Master's Thesis

Computational Science and Engineering
International Master's Program
at the Faculty of Informatics

EFFICIENT SAMPLING FOR ACCELERATED DIFFUSION MAGNETIC RESONANCE IMAGING

Author:	Maryna Babayeva
Examiners:	Prof. Dr. Nassir Navab, Prof. Dr. Dimitri Van De Ville
Advisors:	Dr. Diana C. Mateus, Dr. Yves Wiaux
Date:	August 26, 2011

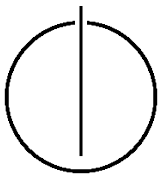

I hereby declare that this thesis is entirely the result of my own work except where otherwise indicated. I have only used the resources given in the list of references.

München, 23. August 2011 Maryna Babayeva

Abstract

Diffusion magnetic resonance imaging (dMRI) is a non-invasive method that allows connectivity mapping of the brain. However, despite major advances in this field, accurate inference of these patterns and its applicability within a clinical context is still in its early stages. This thesis describes a conceptually novel method for reconstructing neuronal pathways inside the brain from diffusion-weighted imaging (DWI) measurements with high angular resolution and short data acquisition time. The proposed method combines recent theoretical advances on spherical sampling and noise-reduction techniques from the field of compressed sensing. Numerical simulations were performed to study the best sampling strategy under a novel sampling theorem on the sphere in order to reduce the acquisition time during dMRI scans. Furthermore, these results were combined with the recently proposed spherical deconvolution technique to reconstruct the distribution of neuronal tracts (or fibers) within one voxel with high angular resolution between multiple crossing fibers. The spherical deconvolution problem was hereby formulated as an inverse problem and solved using techniques adopted from the field of compressed sensing. Since the result of the spherical deconvolution step is sparse in nature, the basis pursuit denoising formulation of the inverse problem is optimal within this context. Finally, the resulting fiber orientation reconstruction was compared with diffusion spectrum imaging (DSI) – a classic model-free acquisition method. Simulations revealed that the proposed approach is superior to DSI in terms of both, acquisition time and angular resolution of crossing fibers ($\geq 40^\circ$ with at least 90% sensitivity). Our investigations showed that the application of spherical deconvolution stated as a basis pursuit denoising problem holds great promise for high angular resolution dMRI.

Acknowledgements

I would like to kindly acknowledge my supervisor at the EPFL, Dr. Yves Wiaux, for his supervision and guidance.

Special thanks goes to Prof. Dimitri Van De Ville and Prof. Bart Deplancke from EPFL for the opportunity to do research and write my thesis within this highly interesting research topic.

I further would like to gratefully and sincerely thank Dr. Alessandro Daducci, post doctoral researcher at EPFL, for his highly valuable scientific contributions and many fruitful discussions.

I would also like to acknowledge Jason McEwen, post doctoral researcher at EPFL (now at University College of London) for his important input, ideas, and guidance during this thesis work. He helped me with understanding the world of spherical harmonics. Many thanks go also to Gilles Puy, a PhD student at EPFL, for his technical support.

Dr. Diana Mateus and Prof. Nassir Navab from the Technical University of Munich, I would like to thank for the rigorous interest in the topic, for supervision and for evaluating and grading this work.

Many thanks to those who did the proof-reading and gave valuable comments to improve this thesis. In particular to Sebastian Waszak, who gave me advices on scientific writing. Most importantly, I would like to thank Sebastian for his endless support, encouragement, and patience. It was undeniably of great value during my whole studies and thesis work.

This thesis work was financially supported by a scholarship from the Siemens Master Program and by the PROMOS scholarship from the Federal Ministry of Education and Research[1] (Germany).

[1] Bundesministerium für Bildung und Forschung

Contents

"The truth is our most precious possession, thus let us be economical in its use."

MARK TWAIN

1 Introduction and Problem Statement

Diffusion magnetic resonance imaging (dMRI) experienced high scientific attention during the past decades. It can help to diagnose tumors or to study psychiatric disorders or neurological diseases in more detail. To visualize the white matter of the brain and the neuronal fiber bundles, diffusion tensor (DT) model is the most commonly used imaging technique to acquire the orientation of the fibers within a voxel. However, this approach does not allow to resolve regions of multiple fiber crossings with different orientations in space as demonstrated in Figure 1.1.

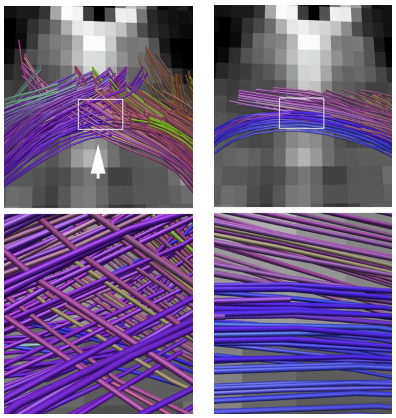

(a) DSI **(b)** DTI

Figure 1.1: Fibers are color-coded according to their orientation, and are superimposed upon a diffusion-weighted image of adjacent cerebral structures. (a) Tractography from diffusion spectrum imaging (DSI) is able to resolve crossing fibers. (b) Failed reconstruction of intersecting fibers with diffusion tensor imaging (DTI). [Wedeen et al., 2008]

Thus, many alternative models have been proposed to improve the angular resolution of dMRI. Some of the methods, which allow high angular resolution diffusion imaging, are diffusion spectrum imaging, Q-ball imaging, and techniques based on spherical deconvolution, just to name few. Please refer to a review by Assemlal et al. [2011] and the book on dMRI by Johansen-Berg and Behrens [2009] for more information on different sampling and reconstruction techniques in dMRI. All these techniques have in common that they are based on

nearly identical sampling schemes. The data acquisition consists of dense sampling, where the orientation distribution function (ODF) is estimated from the signal by making use of various mathematical approaches. The sampling strategy in particular evolved towards the use of multiple spherical shells for signal acquisition, which allowed higher angular resolution of crossing fibers. Table 1.1 summarizes the data acquisition times, number of samples and angular resolution for different dMRI techniques. The motivation for finding an efficient sam-

Table 1.1: Diffusion MRI acquisition techniques. Acquisition times as reported in [Hagmann et al., October 2006]. Angular resolution for q-ball imaging was taken from [Cho et al., 2008].

Sampling Technique	**Gradient strength** $[sec/mm^2]$	**# of samples in q-space** N	**Acquisition time** $[min]$	**Min. angle**
DWI	$b \leq 1000$	$N = 1$	1–3	$N.A.$
DTI	$b \leq 1000$	$N \geq 7$	3–6	$N.A.$
DSI	$b \geq 8000$	$N \geq 200$	15–60	$\approx 45°$
q-ball	$1000 \leq b \leq 3000$	$N \geq 60$	10–20	$\approx 50°$

pling scheme lies in the aim to map effectively the diffusion signal with as few samples as possible, which leads to a reduction of acquisition time. Simultaneously, the angular resolution needs to remain high or even be improved. Within this context, spherical harmonic (SH) transform became a popular mathematical approach, due to its ability to perform convolution operations easier and more efficient in harmonic than in real space. The main drawback of this transformation is, however, that aliasing occurs if the signal is not sampled at a proper bandwidth. According to Daducci et al. [2011] this problem has not been addressed in a quantitative approach yet. Therefore, they proposed a novel multi-shell q-space sampling technique. This technique, as well as, how to model the ODF with the help of spherical harmonics will be presented here in more detail.

The main goal of this thesis was to improve the results of spherical sampling by transforming the ODF to a different form. Hereby, we exploited the nice property of the harmonic space allowing us to perform convolution easily. This is important as we will define an inverse problem from the knowledge that an ODF can be transformed to a fiber orientation distribution function (FOD) by means of spherical deconvolution. Our approach made it possible to extract the fiber directions from the FOD with higher angular resolution from less samples than in DSI.

This thesis is organized in the main chapters: 1 Introduction and Problem Statement, 2 Background, 3 Methods, 4 Results, 5 Discussion, and 6 Conclusion. The Introduction and Problem Statement gives a brief overview over the project and the problem statement. The

chapter Background describes the biological brain tissue that is visualized with dMRI. Further, the history and physics of diffusion and diffusion-weighted imaging is introduced and two reconstruction and visualization techniques (DTI and DSI) are described. The last part of this introductory chapter gives a brief overview on the dMRI applications and the importance of high-angular resolution reconstruction techniques. The Methods chapter introduces the reader to the mathematical background used in this work, including the novel multi-shell sampling, introduction to spherical deconvolution for FOD calculations, and formulation of the inverse problem as a basis pursuit denoising (BPDN) problem with and without noise. The chapter Results presents the outcome of the extensive numerical simulations. Here, we will also propose modifications to the formulation of the BPDN problem. Additionally, we will justify the advantages of our technique and discuss the comparison to DSI. The last part of this thesis work – Discussion and Conclusion – will evaluate the results and deal with open scientific questions and propose further possible direction of this research project.

"If you can't convince them, confuse them!"

HARRY TRUMAN

2 Background

This chapter gives a brief overview on the background of diffusion magnetic resonance imaging (dMRI) and its applications. The following introductory sections are inspired from a book on dMRI by Johansen-Berg and Behrens [2009], work of Hagmann et al. [October 2006], and Beaulieu [2002], and a review article on recent advances in diffusion MRI [Assemlal et al., 2011].

2.1 Diffusion MRI: Theory and Applications

2.1.1 What Are Neuronal Tracts?

Diffusion MRI makes it possible to visualize and to investigate the architecture of the brains white matter. This application relies on the phenomenon that water diffusion is obstructed by barriers created by biological structures inside the brain (e.g., axons, neurons, and glial cells within the brain tissue). Figure 2.1 illustrates the neuronal cell body and the axon.

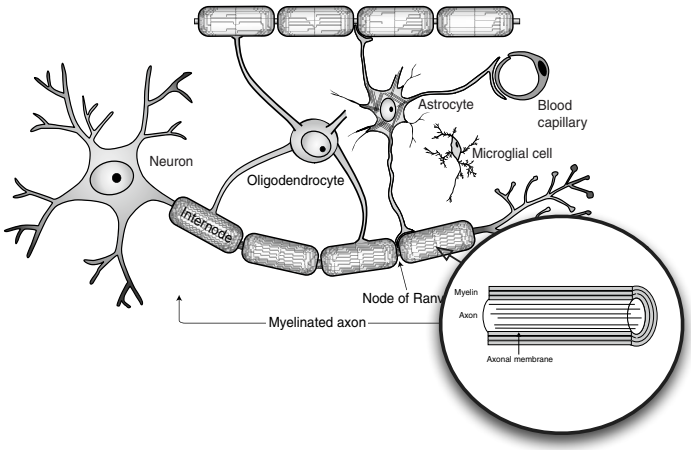

Figure 2.1: Schematic representation of the major cellular elements of the white matter as the neuronal cell body and the axon. [Johansen-Berg and Behrens, 2009]

These are the major structural elements that hinder water diffusion perpendicular to the axons. The axon, embedded in the white matter, is surrounded by a type of fat, called myelin sheath. The myelin lets the white matter appear whitish (see Figure 2.2a). This specialized organization of the myelin sheaths acts as an electrical insulator, and it increases the speed of transmission of nerve signals, whereby electrical impulses are sent along the axon from the neuronal cell body to the axon terminus. The electrical impulse usually affects the cell membrane potential of one of the neuron's dendrites and then travels along the length of this axon to transmit the electrical signal to other neurons. The common term for an axon is nerve fiber and bundles of these fibers are called neuronal tracts or fibers (Figure 2.2c and Figure 2.2b).

(a) Coronal Section **(b)** Right Cerebral Hemisphere **(c)** Left Cerebral Hemisphere

Figure 2.2: Dissections of the human brain [Williams et al., 1997]. In (a) the grey and the white matters can be seen. (b) and (c) show the dissected human brain from the left and from the right side respectively, revealing the structure of the white matter and the fiber bundles.

2.1.2 Physics of Diffusion

Diffusion is a physical process leading to a uniform distribution of particles and thus to the complete mixing of two or more substances. Brown (1827), Fick (1855), and Einstein (1905) explained the theory behind this physical phenomenon and prepared the mathematical basis for further reasearch.

In a medium, where the diffusion of particles is not hindered by anything, it can diffuse equally in all directions and is then called isotropic. However, when the motion of the particles is constrained by surrounding materials such as in biological tissues it is called anisotropic. The differences between isotropic and anisotropic diffusion are illustrated in Figure 2.3.

To characterize the motion of water molecules in the brain qualitatively, previously described observations are used to form a more elaborate formulation of the diffusion phenomenon (see Section 2.1.4 for more details).

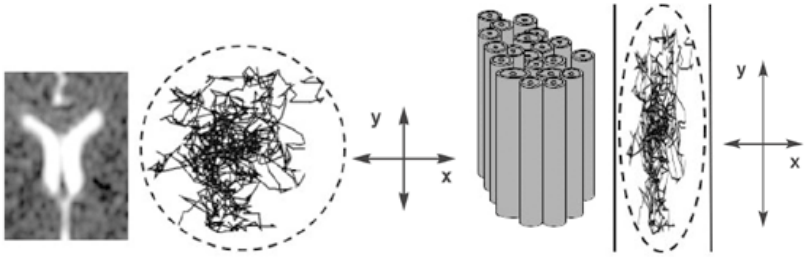

(a) Isotropic diffusion **(b)** Anisotropic diffusion

Figure 2.3: Random motion of a single water molecule due to diffusion in two different tissues of the brain. (a) Isotropic diffusion, e.g., in the cerebrospinal fluid. (b) Anisotropic diffusion due to constraints in vertical direction, e.g., in nerve fibers of the white matter. [Beaulieu, 2002]

2.1.3 Brief History of dMRI

Principles of Nuclear Magnetic Resonance (NMR)
[Bloch, Purcell, Carr (1946), Hahn (1950)]

↓

The Pulse Gradient Spin-Echo (PGSE) sequence
[Stejskal and Tanner (1965)]

↓

Scalar Diffusion-Weighted Imaging (DWI)
[Le Bihan and Breton (1985)]

↓

Diffusion Tensor Imaging (DTI)
[Basser et al, (1992-1994)]

↓

Diffusion Spectrum Imaging (DSI)
[Wedeen et al (2000)]

Figure 2.4: Brief history of diffusion MRI [Descoteaux, 2008].

Diffusion MRI is based on principles of nuclear magnetic resonance (NMR) imaging. NMR is a spectroscopic method to study the electronic environment of individual atoms and the interactions with neighboring atoms. This allows the elucidation of molecular structure and dynamics for concentration measurements. NMR was described at the same time by Bloch [1946] and Purcell et al. [1946], and was awarded by a Nobel Prize in Physics in 1952. Few years after this discovery Carr and Purcell [1954] proposed to create the first one-dimensional

MR image by introducing a gradient to the magnetic field. Shortly afterwards, Hahn [1950] published an article on the NMR spin echo, where he posed the fundamental observation that the amplitude of received signal is reduced after a perturbation of the magnetic field due to random thermal motion of the spins. This phenomenon is a major step towards understanding dMRI. Many more advances in MR imaging followed (see Figure 2.4) and will be described by the following section in more detail.

2.1.4 Acquisition Techniques

2.1.4.1 1-D dMRI: Diffusion Weighted Imaging (DWI)

Diffusion weighted imaging (DWI) was performed for the first time by Wesbey et al. [1984]. A year later DWI acquisition on a hen's egg was done by Taylor and Bushell [1985]. After further development of the technique LeBihan et al. [1986] was finally able to acquire first images of the human brain and he also introduced the famous b-value (see Equation 2.4).

Through the development of DWI it has become possible to determine the movement of water molecules inside the human brain and eventually present this information to understand further the nature of the white matter. The measured signal loss enables a quantitative evaluation of diffusion in gradient direction (Figure 2.5).

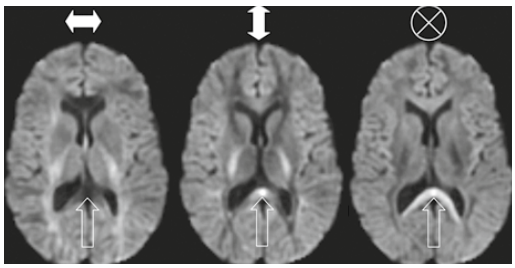

(a) x-direction **(b)** y-direction **(c)** z-direction

Figure 2.5: Effects of changing the axis of the diffusion–encoding gradients on the diffusion–weighted signal intensity. In the area highlighted by the arrows the apparent diffusivity is high along the horizontal axis as shown by (a), but low in the two orthogonal directions, as dark areas represent high apparent diffusivity. [Assemlal et al., 2011]

One DW image corresponds to a single point in a so called q-space, where one q-space sample represent a diffusion weighted signal measured in this direction. To measure diffusion of water molecules qualitatively in a given direction $\mathbf{g} = (g_x, g_y, g_z)$, the gradient spin echo sequence of Stejskal and Tanner [1965] is used. They adopted a T2-weighted spin-echo sequence to measure water diffusion (as illustrated in Figure 2.6). To acquire a diffusion weighted signal,

two gradient pulses $g(t)$ in a diffusion encoding gradient direction $\mathbf{g}$ of a duration δ are used. These gradient pulses are placed symmetrically on both sides of the 180° rephasing pulse. The first gradient pulse leads to a phase shift of the spins. The 180° pulse combined with the second gradient pulse applies another phase shift after a time Δ. The acquired signal caused by stationary molecules is unaffected by this pulse, as the previously applied phase shift is canceled. However, water molecules which moved during the time period Δ experience different phase shifts by the two gradient pulses, resulting in a signal loss, whereas, stationary molecules are unaffected by gradients and measured signal intensity is preserved [Koh and Collins, 2007]. The diffusion displacement probability density function (PDF), sometimes

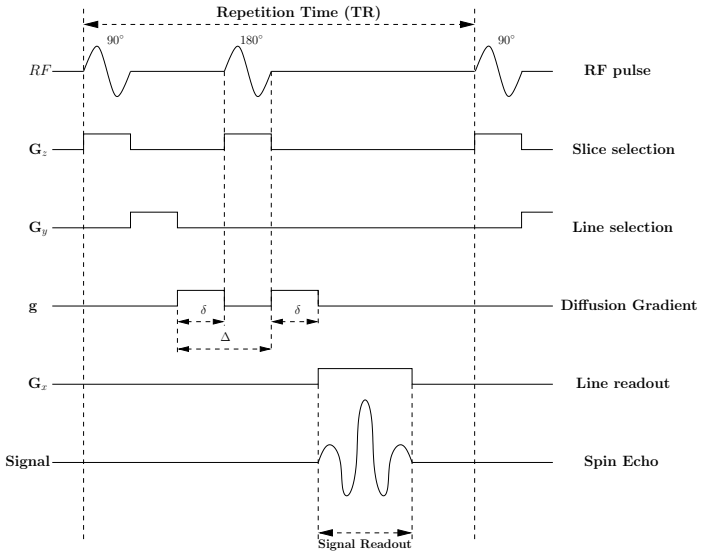

Figure 2.6: Schematic visualization of the Stejskal-Tanner PGSE sequence [Descoteaux, 2008].

also addressed in literature as the diffusion propagator, is denoted by $P(\mathbf{r}, \tau)$ and represents the probability, that a water molecule will experience a certain displacement $\mathbf{r}$ after a time τ. Stejskal and Tanner showed that the signal attenuation $S(\mathbf{q}, \tau)$ has a Fourier relationship with the average diffusion propagator $P(\mathbf{r}, \tau)$.

$$E(\mathbf{q}, \tau) = \frac{S(\mathbf{q}, \tau)}{S_0} = \int P(\mathbf{r}, \tau) e^{2\pi i \mathbf{q}^T \mathbf{r}} d\mathbf{r} = \mathcal{F}_{3D}^{-1}[P](\mathbf{q}), \tag{2.1}$$

Here, the value of the real space vector $\mathbf{q}$ is given by

$$\mathbf{q} = (q_x, q_y, q_z) = \frac{\gamma}{2\pi} \int_0^{\delta} g(t) dt = \frac{\gamma \delta \mathbf{g}}{2\pi}, \tag{2.2}$$

with $\gamma = 42$ MHz/T being the nuclear gyromagnetic ratio for water protons [Westin and

Maier, 2002], $\mathbf{g}$ the applied diffusion gradient vector, and $P(\mathbf{r}, \tau)$ the diffusion PDF or diffusion propagator of water molecules. P is the function, which is aimed to be reconstructed in dMRI. Therefore, the diffusion PDF must be sampled along many $\mathbf{q}$ directions. Thus, the space of all possible $\mathbf{q}$ vectors in three dimensions is called q-space.

By solving the Fourier integral in Equation 2.1 under assumption of a Gaussian PDF analytically, the Stejskal-Tanner signal attenuation equation obtains the commonly used form as follows in Equation 2.3.

$$S(\mathbf{q}, \tau) = S_0 e^{-\tau \mathbf{q}^T D \mathbf{q}},\ S(b, \mathbf{g}) = S_0 e^{-b \mathbf{g}^T D \mathbf{g}}, \tag{2.3}$$

The signal attenuation is also often written with respect to $\mathbf{g}$, with $|\mathbf{g}|$ being strength of the diffusion sensitizing gradient pulses. Here it is common to use the b-value as a diffusion weighting factor:

$$b = \gamma^2 \delta^2 (\Delta - \delta/3) |\mathbf{g}|^2 = (2\pi)^2 (\Delta - \delta/3) |\mathbf{q}|^2, \tag{2.4}$$

thus, the signal attenuation is obtained with respect to the b-value given by Equation 2.4. The covariance matrix D of the net displacement vector $\mathbf{r}$ was defined by Einstein as $D = \frac{1}{6\tau} \langle \mathbf{r}^T \mathbf{r} \rangle$, where τ is the diffusion time and $\langle \dots \rangle$ denote an ensemble average of $\mathbf{r}$.

2.1.4.2 3-D dMRI: Diffusion Tensor Imaging (DTI)

To describe the diffusion process in a 3-dimensional space a diffusion tensor model (DT) as proposed by Basser et al. [1994] can be used. This tensor is obtained by solving the Stejskal-Tanner equation 2.3. A log is taken on both sides and the equation is solved for six unknowns (entries of D) at each voxel. At least seven images with non-coplanar gradient directions including S_0 for normalization must be acquired to calculate six tensor components.

$$\mathbf{g}^T D \mathbf{g} = \frac{\log S_0 - \log S}{b}, \tag{2.5}$$

$$\begin{bmatrix} \ln S_1 \\ \ln S_2 \\ \vdots \\ \ln S_m \end{bmatrix} = \begin{bmatrix} 1 & -b_1^{xx} & -b_1^{yy} & \cdots & -b_1^{xz} \\ \vdots & \vdots & \vdots & \ddots & \vdots \\ 1 & -b_m^{xx} & -b_m^{yy} & \cdots & -b_m^{xz} \end{bmatrix} \begin{bmatrix} \ln S_0 \\ D_{xx} \\ D_{yy} \\ \vdots \\ D_{xz}. \end{bmatrix} \tag{2.6}$$

The DT formalism allows the extraction of some interesting properties of diffusion. Therefore, the tensor is decomposed into its three eigenvalues λ_1, λ_2, and λ_3, where $\lambda_1 \geq \lambda_2 \geq \lambda_3$, and

corresponding eigenvectors ν_1, ν_2, ν_3.

$$D = \begin{bmatrix} D_{xx} & D_{xy} & D_{xz} \\ D_{xy} & D_{yy} & D_{yz} \\ D_{xz} & D_{yz} & D_{zz} \end{bmatrix} \tag{2.7}$$

The largest eigenvalue λ_1 gives the principal direction of the DT ν_1 and the other two eigenvectors span the orthogonal plane to it (illustrated in Figure 2.7).

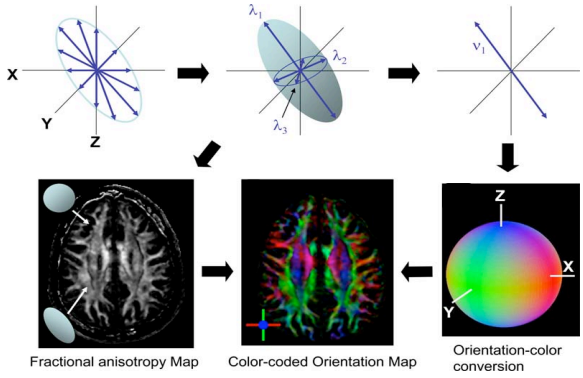

Figure 2.7: The principle of DTI and contrast generation from diffusion measurements along multiple axes. [Mori and Zhang, 2006]

From this eigenvalue decomposition, several rotationally invariant quantities can be extracted such as the mean diffusivity $\bar{\lambda}$ with $3\bar{\lambda} = \lambda_1 + \lambda_2 + \lambda_3$ or the fractional anisotropy (FA) as defined by Equation 2.8. A typical value for FA is approximately 0.8, as measured by Mori and Zhang [2006]. Figure 2.8b presents how the tensor shape affects the FA value.

$$FA = \frac{3}{\sqrt{2}} \frac{\sqrt{Var(\lambda)}}{\sqrt{\lambda_1^2 + \lambda_2^2 + \lambda_3^2}} \tag{2.8}$$

with

$$Var(\lambda) = \frac{(\lambda_1 - \bar{\lambda})^2 + (\lambda_2 - \bar{\lambda})^2 + (\lambda_3 - \bar{\lambda})^2}{3}. \tag{2.9}$$

Most often the FA map itself is used to visualize the regions of anisotropy, as can be seen in Figure 2.8a. It is also common to visualize the DTs with a Red-Blue-Green (RGB) colormap as proposed by Pajevic and Pierpaoli [1999]. The RGB map encodes the 3–dimensional coordinates of the principal eigenvector ν_1, which is assumed to represent the local fiber orientation (Figure 2.7). The areas of red, blue and green color indicate tensors aligned with the x, y, z directions in space. Further, the dark regions are isotropic, meaning the tensor shape is spherical and bright regions are anisotropic leading to an elongated shape of the tensor. Even though the DT is a powerful tool for many clinical applications, the DT model

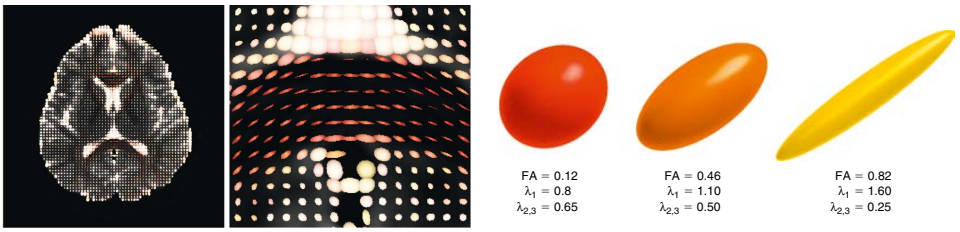

(a) DTI ellipsoids **(b)** Fractional anisotropy

Figure 2.8: Ellipsoidal visualization of diffusion tensor data. (a) shows on the left the whole view and on the right a zoomed view at the splenium of corpus callosum [Masutani et al., 2003]. (b) illustrates diffusion ellipsoids with different fractional anisotropy ranging from almost isotropic (lower FA) to anisotropic (higher FA) diffusion profile [Johansen-Berg and Behrens, 2009].

is limited. It cannot be used to visualize voxels with multiple fiber crossings. This limitation is caused by the assumption of the Gaussian PDF and the limited number of degrees of freedom in the model. Hence, we need higher order models to be able to describe non-Gaussian distributions.

2.1.4.3 3-D dMRI: Diffusion Spectrum Imaging (DSI)

In contrast to DTI, diffusion spectrum imaging (DSI) is not based on any model hypothesis on the diffusion. It is also said to be model-free. In DSI, the resolution of the diffusion PDF depends only on the number of samples in q-space. Equation 2.10 shows the way of extracting the diffusion PDF from data measuring the signal on a Cartesian grid of points in q-space and then taking the 3-dimensional Fourier transform to obtain the PDF.

$$P(\mathbf{r},\tau) = \int E(\mathbf{q},\tau) e^{-2\pi i \mathbf{q}^T \mathbf{r}} d\mathbf{q} = \mathcal{F}_{3D}[E](\mathbf{r}) \tag{2.10}$$

DSI was described for the first time by Wedeen [2000]. The original technique has, however, some technical limitations. In order to achieve a high resolution, a big sampling box with many q-space sampling directions is required. This needs many measurements and very large b-values. This results in a major practical problem, because of the large number of samples. The acquisition time then increases drastically, hence making it impractical to use in a clinical context (up to 60 minutes for data acquisition). For DSI, usually 515 diffusion-weighted images are acquired in q-space with b-values ranging from 0 sec/mm^2 to $8,000$ sec/mm^2. Then a Fourier transform is applied to the obtained q-space data to calculate the PDF.

As a result of DSI limitations, other techniques have been developed to calculate the desired diffusion PDF. One such feasible approach is Q-ball imaging developed by Tuch [2004] (Figure

2.9a). This imaging technique has again the advantage of being model independent, and it has been shown that it is possible to reconstruct the diffusion orientation distribution function (ODF) directly from samples placed on a single spherical shell in q-space.

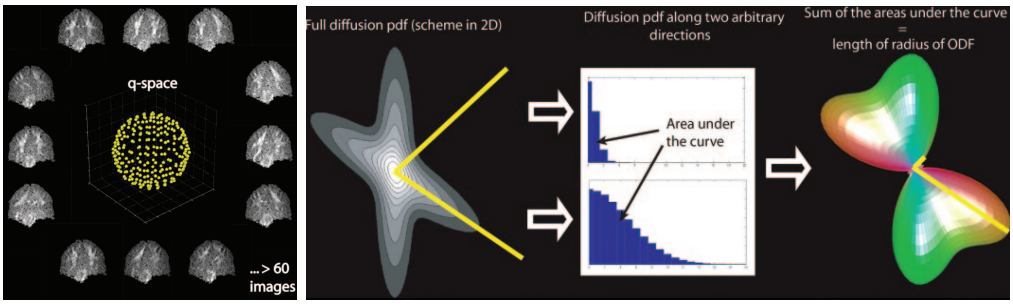

(a) Q-ball sampling **(b)** From PDF to ODF

Figure 2.9: (a) shows that in q-ball imaging, points on a shell with a constant b-value are acquired in q-space. At least 60 images are necessary to reconstruct an orientation distribution function that is realistic. (b) gives an overview on how to compute an ODF from acquired PDF by integrating the area under the curve of the exponential decay of the PDF. [Hagmann et al., October 2006]

Figure 2.9 shows how an ODF is computed from the PDF and visualized. The values of the displacement distribution along diffusion directions (yellow lines in Figure 2.9b) are represented as histograms. The ODF is then computed along them by calculating the area under the diffusion propagator curve for each of the sampling directions. The integral is then visualized by a deformed sphere, where the different lengths of the two radii correspond to the magnitude of diffusion in the respective direction.

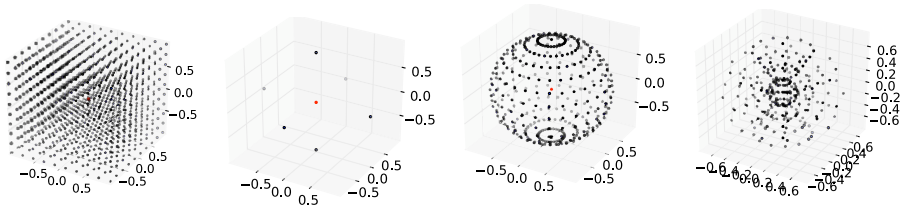

(a) DSI **(b)** DTI **(c)** Q-ball **(d)** Sparse sampling

Figure 2.10: Different sampling schemes of the q-space [Assemlal et al., 2011].

Other acquisition techniques allowing high angular resolution diffusion imaging (HARDI) also exist. For more technical details on q-ball and other acquisition and imaging techniques the reader may refer to recently published literature (e.g., Assemlal et al. [2011]). Figure 2.10 gives an overview on some of the q-space sampling schemes.

2.2 Clinical and Basic Research Applications

Moseley et al. [1990] showed that water diffusion in cerebral tissue decreases within minutes after a stroke in brains of cats. This finding quickly attracted a lot of attention as a method for early detection of brain injuries, because it is not possible to show stroke for hours to days after the onset of injury with standard imaging methods. Also, in the assessment of tumors, dMRI was identified as a useful imaging tool. Tumors are more cellular than the tissue from which they originate and appear with different signal intensity due to restricted diffusion in DWI [Koh and Collins, 2007]. Now, with dMRI being established in stroke and tumor diagnosis, the way was paved for further research on other potential applications for dMRI. Large scale research projects have been initiated to study the human brain with this new imaging technique[1,2]. Nowadays, a major application area of dMRI is fiber-tracking or 'tractography' (see Figure 2.11a). The field of tractography has undergone intensive development since the introduction of dMRI and exciting applications are now beginning to emerge e.g., assessment of brain maturation in children [Schmithorst and Yuan, 2010] or monitoring of disease progression [Hagmann et al., 2008].

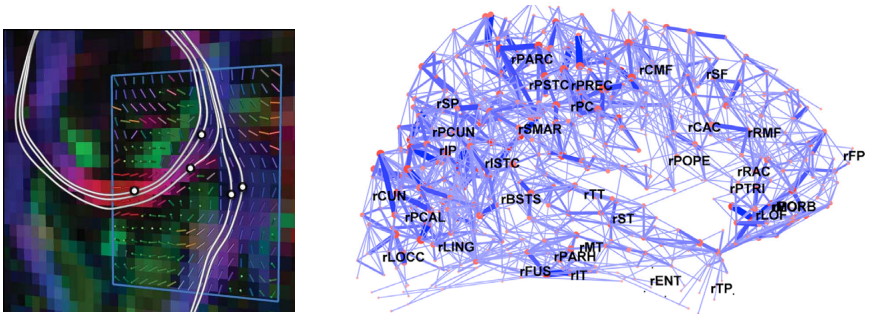

(a) **(b)**

Figure 2.11: (a) Deterministic streamline tractography from a DTI model. White lines show the fiber tracts based on the directions, reconstructed from each voxel [Tournier et al., 2011]. (b) Lateral view of the connectivity map of the right hemisphere of a human brain from DSI [Hagmann et al., 2008].

Tractography for itself again lead to very interesting applications to build large-scale structural brain networks [Hagmann et al., 2008]. Such networks provide information on how brain regions, responsible for different tasks, are interconnected (see Figure 2.11b). Connectivity-mapping hold great promise for studies of psychiatric disorders or neurological diseases as multiple sclerosis, Alzheimer's disease, or schizophrenia from a new perspective [LeBihan, 2003].

[1] http://www.brain-connect.eu/
[2] http://www.humanconnectomeproject.org/

"It is amazing what you can accomplish if you do not care who gets the credit."

HARRY TRUMAN

3 Methods

3.1 Novel MWS Sampling Theorem and Spherical Harmonics

To represent discrete data, that lives on a sphere, the spherical harmonic (SH) basis is known to be an appropriate concept. Spherical harmonics Y_{lm} of order l and degree m are the angular portions of Laplace's equation in spherical coordinates. They are defined as

$$Y_{lm}(\theta,\phi) = \sqrt{\frac{2l+1(l-m)!}{4\pi(l+m)!}} P_{lm}(\cos\theta) e^{im\phi} \tag{3.1}$$

and will be used for all further data representations, with P_{lm} being the associated Legendre functions. With the spherical harmonics forming a complete, orthogonal basis on the sphere, any square integrable function on the sphere (e.g., ODF) may be represented by a harmonic expansion such as.

$$f(\theta,\phi) = \sum_{l=0}^{\infty} \sum_{m=-l}^{l} f_{lm} Y_{lm}(\theta,\phi). \tag{3.2}$$

Here, the spherical harmonic coefficients f_{lm} are given by a projection to the spherical harmonic basis functions Y_{lm}. To perform the exact SH-transform efficiently, an implementation of McEwen and Wiaux [in press] will be used.

The essence of spherical sampling on multiple shells, as introduced by Daducci et al. [2011], lies in the fact, that on each shell, the signal E is being sampled according to the novel MWS (McEwen & Wiaux symmetric) sampling theorem using equiangular grids [McEwen and Wiaux, in press]. This approach allows an exact computation of B^2 SH coefficients of a function on the sphere of band limit B on the basis of $(B-1)(2B-1)+1 \sim 2B^2$ samples. In contrast to MWS sampling technique, another exact equiangular sampling theorem by Driscoll and Healy [1994] needs at least $4B^2$ samples to obtain the signal on a sphere and avoid aliasing effects. The new sampling technique gives a big benefit in terms of acquisition time, as less samples are required (see Figure 3.1a for comparison).

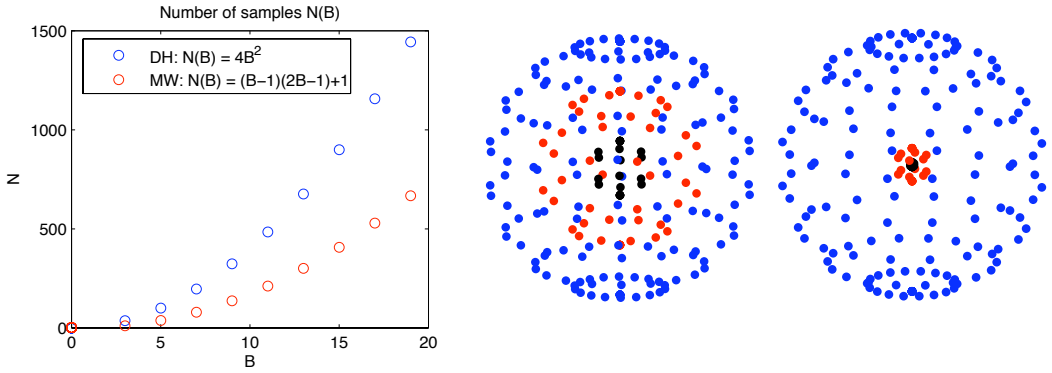

(a) Number of samples **(b)** Linear sampling **(c)** Logarithmic sampling

Figure 3.1: (a) shows the number of samples needed to reconstruct a signal without aliasing according to the Driscoll–Healy (DH) theorem versus the MWS sampling scheme. (b) and (c) show linear and logarithmic distribution of shells in q-space.

In order to map the b-value to the required bandlimit B, while keeping the aliasing low, a so called dictionary, created from simulations with different FAs, is used (Figure 3.2). The b-value provides information on where such a sampling shell is located in q-space to measure the exponential decay of the signal E. Two approaches of where to put the shells will be investigated in this work: logarithmic and linear placements (Figure 3.1c and Figure 3.1b).

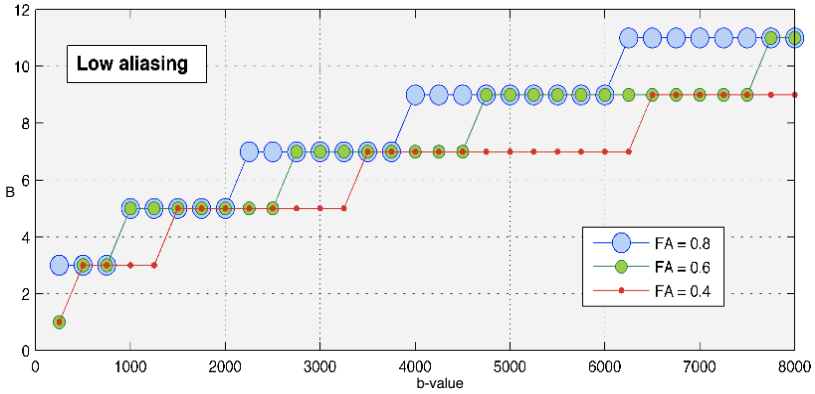

Figure 3.2: Values of bandlimit B required to describe the diffusion signal E at each b-value for a low aliasing level and different FA [Daducci et al., 2011].

Although, the exact MWS sampling theorem provides a good guideline to set up the sampling scheme to keep angular aliasing low (i. e., how many samples on each shell), the radial aliasing problem remains (i. e., where to put the shells).

3.1.1 Orientation Distribution Function (ODF)

To define the orientation distribution function (ODF) the probability of diffusion in the direction $\hat{r}$ through a solid angle element $d\Omega$ will be denoted as $O(\hat{r})d\Omega$. The ODF is computed by integrating the displacement probabilities $P(\mathbf{r})$ as in Equation 3.5.

$$P(\mathbf{r})dv = P(r\hat{r})r^2 dr d\Omega \tag{3.3}$$

$$O(\hat{r})d\Omega = \int_0^\infty P(r\hat{r})r^2 dr d\Omega \tag{3.4}$$

$$O(\hat{r}) = \int_0^\infty P(r\hat{r})r^2 dr \tag{3.5}$$

As proposed by Aganj et al. [2009], the factor r^2 must be considered, when integrating the propagator. The diffusion of water molecules $P(\mathbf{r})$ gives the displacement probability $P(\mathbf{r})dv$ of a molecule to move from an initial location at the origin to the infinitesimal volume element $dv = dxdydz$ located at $\mathbf{r} = (x, y, z)^T$ after a certain amount of time (Equation 3.3).

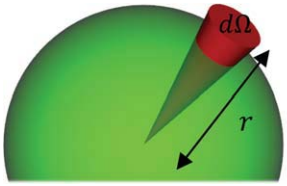

Figure 3.3: Radial integration of the PDF in a cone of constant solid angle [Aganj et al., 2010].

In spherical coordinates, which are parameterized by (r, θ, ϕ) with

$$\mathbf{r} = r\hat{r} \text{ and } \hat{r}(\theta, \phi) = (\sin\theta\cos\phi, \sin\theta\sin\phi, \cos\theta)^T, \tag{3.6}$$

the volume element is

$$dv = r^2 dr d\Omega \text{ with } d\Omega = \sin\theta d\theta d\phi \tag{3.7}$$

being the infinitesimal solid angle element (see Figure 3.3 for visual representation). Therefore, the r^2 factor is important for ODF calculations.

For simulation purposes, the following PDF, as a finite mixture of Gaussians for N crossing fibers with the diffusion tensor D_i will be assumed. This approach was proposed by Tuch

[2002] and is defined as:

$$P(\mathbf{r}) = \sum_i^N \frac{f_i}{(2\pi)^{2/3}\sqrt{\det D_i}} e^{-1/2\mathbf{r}^T D_i^{-1}\mathbf{r}} \tag{3.8}$$

with total diffusion

$$\int P d\mathbf{r} = 1 \implies \sum_i f_i = 1, \tag{3.9}$$

and f_i being the volume fraction in the i^{th} direction. The ODF is formulated as in Equation 3.10 and will be referred to as *true* ODF or $O_{true}(\hat{r})$ in the remainder of this work, i. e.,

$$\begin{aligned} O_{true}(\hat{r}) &= \int P(r\hat{r}) r^2 dr \\ &= \sum_i^N \frac{f_i}{(2\pi)^{2/3}\sqrt{\det D_i}} \int e^{-1/2r^2\hat{r}^T D_i^{-1}\hat{r}} r^2 dr. \end{aligned} \tag{3.10}$$

With the Gaussian integral $\int x^2 e^{-ax^2} dx = \frac{\sqrt{\pi}}{4a^{3/2}}$, the above Equation 3.10 is solved to obtain the final formulation of the ODF (see A.1 for proof), i. e.,

$$O_{true}(\hat{r}) = \sum_i^N \frac{f_i}{4\pi\sqrt{\det D_i}} (\hat{r}^T D_i^{-1} \hat{r})^{-3/2}. \tag{3.11}$$

3.1.2 From dMRI Signal to the ODF

After the signal E is sampled in the previously described way, the ODF can be calculated, as schematically visualized in Figure 3.4.

$$\boxed{E(\mathbf{q})} \longrightarrow \boxed{S(\hat{q})} \xrightarrow{\Lambda} \boxed{\tilde{S}_{lm}} \longrightarrow \boxed{O_{lm}} \xrightarrow{\Lambda^{-1}} \boxed{O(\hat{r})}$$

Figure 3.4: Flow chart representation of the necessary transformations to obtain the ODF from the acquired diffusion signal on the sphere. Λ stands for spherical harmonic transform and Λ^{-1} for the inverse spherical harmonic transform respectively.

For the transformations from Figure 3.4 the famous Fourier relation between the propagator P and the signal E

$$E(\mathbf{q}) = E(q\hat{q}) = \mathcal{F}_{3D}^{-1}[P](\mathbf{q})$$

is used. Here, the relation between ΔE and inverse Fourier transform of P is important. From basic Fourier analysis we know that $\mathcal{F}^{-1}[x^n f](\xi) = \left(\frac{i}{2\pi}\right)^n \frac{\partial^n \hat{f}(\xi)}{\partial \xi^n}$ with $\hat{f}(\xi) = \int f(x) e^{-2\pi i x\xi} dx$.

Thus, we can derive how the diffusion signal E relates to the propagator P, when we incorporate the r^2 factor.

$$\begin{aligned}
\mathcal{F}_{3D}^{-1}[r^2 P](\mathbf{q}) &= \left(\frac{i}{2\pi}\right)^2 (\frac{\partial^2}{\partial q_x^2} + \frac{\partial^2}{\partial q_y^2} + \frac{\partial^2}{\partial q_z^2}) E(\mathbf{q}) && (3.12)\\
&= -\frac{1}{4\pi^2}\Delta E(\mathbf{q}) && (3.13)\\
&= \tilde{E}(\mathbf{q}) && (3.14)
\end{aligned}$$

Our next goal is to find the mathematical formulation for the ODF in harmonic space. Canales-Rodriguez [2009] proposed the use of an intermediate variable S to find the definition of the harmonic coefficients of the ODF in terms of the diffusion signal E, i. e.,

$$\begin{aligned}
S(\hat{q}) &= \int \tilde{E}(\mathbf{q}) d\mathbf{q} && (3.15)\\
&= \int \tilde{E}(q\hat{q}) q dq. && (3.16)
\end{aligned}$$

The Laplacian in spherical coordinates is given by Equation 3.18 with the Laplace-Beltrami operator Δ_b from Equation 3.17. The proof is presented by Aganj et al. [2010].

$$\Delta E(q,\theta,\phi) = \frac{1}{q}\frac{\partial^2}{\partial q^2}(qE) + \frac{1}{q^2}\Delta_b E \tag{3.17}$$

$$\Delta_b = \frac{1}{\sin^2\theta}\frac{\partial^2}{\partial\phi^2} + \frac{1}{\sin\theta}\frac{\partial}{\partial\theta}\left(\sin\theta\frac{\partial}{\partial\theta}\right) \tag{3.18}$$

By integrating the first term of the Laplacian $\frac{1}{q}\frac{\partial^2}{\partial q^2}(qE)$, we can see that it is constant and independent of E with the assumption that the diffusion signal and its derivative go to zero at $q \to \infty$ and by use of the product rule, as presented by the following proof:

$$\begin{aligned}
\int \frac{1}{q}\frac{\partial^2}{\partial q^2}(qE) q dq &= \int \frac{\partial^2}{\partial q^2}(qE) dq\\
&= \left[\frac{\partial}{\partial q}(qE)\right]\\
&= \left[E + qE'\right]_0^\infty\\
&= E(\infty) - E(0) + qE'(\infty) - qE'(0)\\
&= -1 && (3.19)
\end{aligned}$$

Now, with the proof from 3.19 and the Equation 3.16 we obtain the final formulation for $S(\hat{q})$, i. e.,

$$\begin{aligned} S(\hat{q}) &= \int \tilde{E}(q\hat{q})qdq \\ &= \int \frac{\Delta E(q\hat{q})}{-4\pi^2}qdq \\ &= -\frac{1}{4\pi^2}\int \left(\frac{1}{q}\frac{\partial^2}{\partial q^2}(qE) + \frac{1}{q^2}\Delta_b E\right) qdq \\ &= \frac{1}{4\pi^2} - \frac{1}{4\pi^2}\int \frac{1}{q}\Delta_b E dq \\ &\approx \frac{1}{4\pi^2} - \frac{1}{4\pi^2}\Delta_b \underbrace{\int \frac{(E-1)}{q}dq}_{\bar{S}(q)}. \end{aligned} \tag{3.20}$$

Equation 3.20 contains an approximation which is needed, as the integral cannot be calculated for $\frac{E(0)}{q}$ with $E(0) = 1$. The intermediate variable $\bar{S}$ will be then transformed to harmonic space with $\Delta_b Y_{lm} = -l(l+1)Y_{lm}$, according to Equation 3.21.

$$\begin{aligned} \Delta_b \bar{S} &= \Delta_b \sum_{lm} \bar{S}_{lm} Y_{lm}(\theta, \phi) \\ &= -\sum_{lm} l(l+1)\bar{S}_{lm} Y_{lm}(\theta, \phi) \end{aligned} \tag{3.21}$$

From Equation 3.20 and 3.21 follows the definition of the harmonic coefficients of S.

$$S_{lm} = \frac{1}{2\pi^{3/2}}\delta_{l0}\delta_{m0} + \frac{1}{4\pi^2}l(l+1)\bar{S}_{lm} \tag{3.22}$$

The harmonic coefficients of S are related as by Equation 3.23 to form the definition of the ODF in harmonic space,

$$O_{lm} = \frac{1}{2\sqrt{\pi}}P_l(0)\frac{S_{lm}}{S_{00}} \tag{3.23}$$

$$\begin{aligned} &= \frac{1}{2\sqrt{\pi}}P_l(0)\left(\delta_{l0}\delta_{m0} + \frac{1}{2\sqrt{\pi}}l(l+1)\bar{S}_{lm}\right) \\ &= \frac{\delta_{l0}\delta_{m0}}{2\sqrt{\pi}} + \frac{l(l+1)}{4\pi}P_l(0)\bar{S}_{lm} \end{aligned} \tag{3.24}$$

where P_l are the Legendre polynomials with $P_0(0) = 1$ and $S_{00} = \frac{1}{2\pi^{3/2}}$ [Canales-Rodriguez, 2009]. To obtain the ODF $O(\hat{r})$ in real space, the inverse harmonic transform is applied to the harmonic coefficients O_{lm}.

3.2 Fiber Orientation Distribution (FOD) and Spherical Deconvolution

3.2.1 Fiber Orientation Distribution Function

The fiber ODF is another representation of the ODF, which describes the fiber orientation distribution (FOD), in literature sometimes also referred to as fODF. This is motivated by the assumption that a DW signal can be modeled by a single response function. Tournier et al. [2004] proposed a method to extract such an FOD from the ODF by means of spherical deconvolution as illustrated in Figure 3.5.

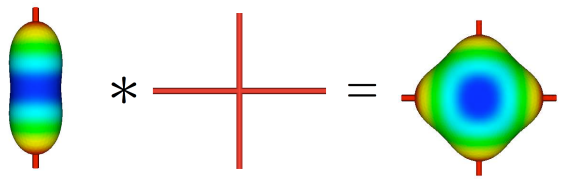

(a) τ **(b)** FOD **(c)** ODF

Figure 3.5: Schematic representation of the convolution between the ODF template τ and true FOD, which results in an ODF [Descoteaux, 2008].

The equation for the FOD is formulated as

$$\bar{O}(\hat{r}) = \sum_i \alpha_i \delta(\hat{r}_i \hat{r} - 1), \tag{3.25}$$

where the relation between the ODF and FOD is described as in Equation 3.26. Here, an ODF equals a convolution of rotated template ODF τ with the FOD $\bar{O}$, i. e.,

$$\begin{aligned} O(\hat{r}) &= \langle R(\hat{r})\tau \mid \bar{O} \rangle \\ &= \sum_i \alpha_i [R(\hat{r}_i)\tau](\hat{r}). \end{aligned} \tag{3.26}$$

The ODF in spherical harmonic coefficients O_{lm} can be described in terms of the harmonic coefficients of the FOD $\bar{O}_{lm}$. The convolution in real space is performed as a multiplication in harmonic space as denoted by the Equation 3.27. For further operations $\bar{O}_{lm}$ and O_{lm} will

be transformed into a vector form and will be then referred to as $\bar{o}_h$ and o_h respectively:

$$O_{lm} = \underbrace{\sqrt{\frac{4\pi}{2l+1}}\tau_{l0}^*}_{T}\bar{O}_{lm} \tag{3.27}$$

$$\Downarrow$$

$$o_h = T\bar{o}_h. \tag{3.28}$$

3.2.2 Inverse Problem and Basis Pursuit Denoising (BPDN)

As described in the previous section, the harmonic coefficients of the FOD can be reconstructed from the ODF with a template operator T. T is created from a single-fiber true ODF simulated by applying the novel efficient sampling scheme on multiple shells and transforming the result to an ODF.

The inverse problem is then redefined as denoted by Equation 3.29. The motivation to use this formulation of the inverse problem is that we expect a sparse solution. The FOD is assumed to be a signal on the sphere in real space with only as many peaks as fiber directions, which is the reason to use a sparsity prior. This basis pursuit denoising (BPDN) problem will be solved by minimization of the l_1-norm under a constraint on the l_2-norm as defined by Chen et al. [1995], i. e.,

$$\begin{aligned} &\text{minimize} && \|\Lambda^{-1}\bar{o}_h\|_1 \\ &\text{subject to} && \|o_h - T\bar{o}_h\|_2 < \varepsilon. \end{aligned} \tag{3.29}$$

BPDN solves a regularized problem with a trade-off between making $T\bar{o}_h$ close to o_h in the l_2 sense and keeping $\bar{o}_h$ sparse in the l_1 sense. Therefore, the template operator T and the inverse harmonic transform operator Λ^{-1} will be taken as the input. Additionally, the adjoint (conjugate transpose) operators T^+ and $(\Lambda^{-1})^+$ are needed by the BPDN solver. As T is zero for odd l, the respective entries must not be taken into account, as division by zero would occur. Additionally, the inverse problem was solved only for the symmetric entries of $\bar{O}_{lm}$ (i. e., for $m \geq 0$), as the FOD as well as the ODF is known to be an antipodally symmetric function on the sphere. Thus, additional operators for adding (ADD) and removing (REM) those zero and symmetric entries have been created. These operators transform the number of coefficients N of the signal according to $N(B) = \frac{B^2}{4} + \frac{B}{2} - \frac{3}{4}$ for odd B. The inverse problem will then be solved for a reduced size vector $\bar{o}_h$. The transformation of the index h for the spherical harmonic coefficients are applied as by $h = 1 + (l^2 + l + m)$ for the vector indices. Please refer to Figure 3.6 for index transformations between the harmonic lm-coefficients and the vector index h. In addition to the described operators, weights $w_i = \sin\theta_i$ need to be applied for the l_1 minimization. These weights are needed because the the l_1-norm is being

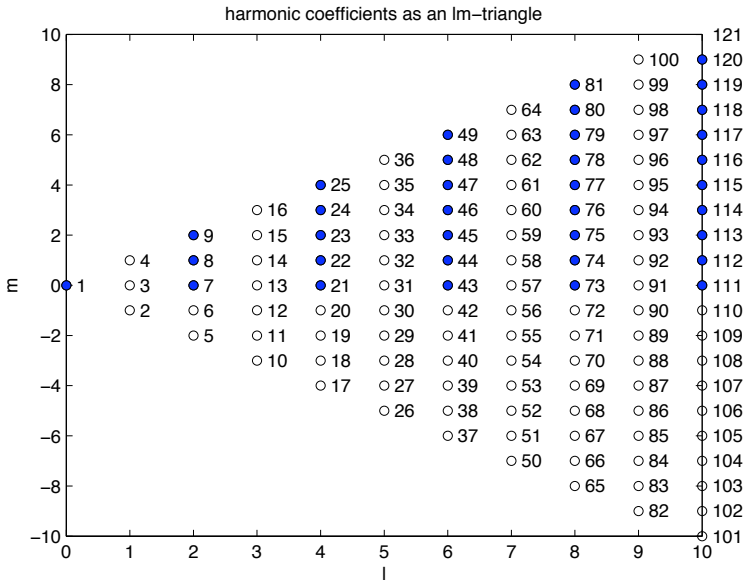

Figure 3.6: Here the index transformation of the harmonic coefficients are shown. Blue circles represent the coefficients, which remain after applying the REM operator. The white circles are added, when the ADD operator is being applied.

calculated on the sphere. The weights are defined as

$$\int |f(r)| d\Omega \approx \sum_i |f(r)| \sin\theta_i, \tag{3.30}$$

with $d\Omega = \sin\theta d\theta d\phi$. We then solve the inverse problem in a following way

$$\begin{aligned} &\text{minimize} && \|w\Lambda^{-1} ADD(\bar{o}_h)\|_1 \\ &\text{subject to} && \|REM(o_h) - REM(T)\bar{o}_h\|_2 < \varepsilon. \end{aligned} \tag{3.31}$$

The resulting harmonic coefficients of the FOD correspond to $\bar{O}_{lm}$ for $m \geq 0$ and even l only. The final result, namely the FOD in real space, is defined as

$$\bar{O} = \Lambda^{-1} ADD(\bar{o}_h).$$

In the remainder of this work the operators REM and ADD as well as the weights won't be shown in the formulation of the inverse problem for simplicity reasons, although they are always being incorporated when the BPDN solver is being applied. Now, we can summarize the above modifications again as a flowchart to visualize the mathematical steps in Figure 3.7.

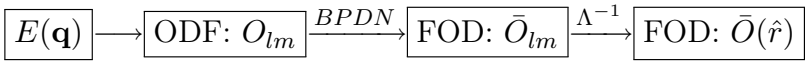

Figure 3.7: Flow chart representation of the necessary transformations to obtain the FOD from the acquired diffusion signal E on the sphere and by spherical deconvolution with BPDN. Λ^{-1} denotes the inverse spherical harmonic transform.

3.3 Adding Rician Noise to the dMRI Signal

It is known that noise in MR data follow a Rician distribution [Jones and Basser, 2004]. Rician noise was applied to each sample of the signal E, where $E(0)$ is the signal intensity measured with no diffusion weighting at $b = 0s/mm^2$. σ_G is the standard deviation for the Gaussian distribution.

$$\sigma_G = \frac{E(0)}{SNR} = \frac{1}{SNR}$$

$$E_n = \sqrt{(E + n_0)^2 + n_1^2}, \text{ where } \{n_0, n_1\} \sim \mathcal{N}(0, \sigma_G)$$

3.3.1 Whitening a Complex Random Vector

The assumption of a χ^2 distribution of the noise holds only for uncorrelated noise with zero mean i. e., whitened noise. This prior knowledge about the noise will be of use later for setting an upper bound for the data constraint of the inverse problem. Rician noise has been simulated without signal and has been modified in the same manner as the signal E to obtain the correlated noise on the harmonic coefficients of the ODF. From sufficiently many such simulations the whitening operator W and the mean of the noise μ have to be calculated. For whitening a vector n with mean μ and covariance matrix C following calculations are needed with Λ being a diagonal matrix of eigenvalues of the covariance matrix C, i. e.,

$$C = E\Lambda E^T \tag{3.32}$$

$$\mathbf{w} = \Lambda^{-1/2} E^T (n - \mu). \tag{3.33}$$

Thus, the output of this transformation has expectation $\mathbb{E}$

$$\mathbb{E}\{\mathbf{w}\} = \Lambda^{-1/2} E^T (\mathbb{E}\{n\} - \mu) = \Lambda^{-1/2} E^T (\mu - \mu) = 0 \tag{3.34}$$

and covariance matrix

$$\begin{aligned}\mathbb{E}\{\mathbf{w}\mathbf{w}^T\} &= \mathbb{E}\{\Lambda^{-1/2}\,E^T\,(n-\mu)(n-\mu)^T E\,\Lambda^{-1/2}\,\}\\ &= \Lambda^{-1/2}\,E^T\,\mathbb{E}\{(n-\mu)(n-\mu)^T\}E\,\Lambda^{-1/2}\\ &= \Lambda^{-1/2}\,E^T\,CE\,\Lambda^{-1/2}\end{aligned} \tag{3.35}$$

By diagonalizing C, we get the following:

$$\Lambda^{-1/2}\,E^T\,E\Lambda E^T E\,\Lambda^{-1/2} = \Lambda^{-1/2}\,\Lambda\,\Lambda^{-1/2} = I. \tag{3.36}$$

Thus, with the above transformation, we can whiten the complex random vector. The whitening operator W for this transformation can be calculated by means of the Cholesky decomposition, i. e.,

$$C = E\Lambda E^T \tag{3.37}$$
$$\Lambda = \Lambda^{1/2}\Lambda^{1/2} \tag{3.38}$$
$$W = \Lambda^{-1/2}E \tag{3.39}$$
$$C^{-1} = W^+W \tag{3.40}$$

In the end we should get a white random vector w with zero mean and the identity covariance matrix.

3.3.2 Setting ε for the Data Constraint of the BPDN Problem

In order to be able to set an upper bound on the data constraint of the minimization problem, we need to estimate ε. To do so we must know the statistics of the noise n. A complex random noise n is proportional to χ^2 with N complex degrees of freedom. A 'complex degree of freedom' is like two real degrees of freedom. However, the distribution is not the usual χ^2 density function with $2N$ degrees of freedom. Each of the real variables going into the computation of n has variance 1/2 [Fuhrmann, 1999]. A complex-valued random variable $n_b = n_b^{(re)} + n_b^{(im)}$ is a complex variable that follows a Gaussian distribution, if its real and imaginary parts, $n_b^{(re)}$ and $n_b^{(im)}$ are jointly Gaussian, uncorrelated, and they have the same variance of σ^2. Denoting the mean of $n_b^{(re)}$ and $n_b^{(im)}$ by μ_{re} and μ_{im} respectively, $\mu = \mu_{re} + \mu_{im} = E[n_b]$ is called the mean of n_b, and σ is called n_b's variance per real dimension.

$$\sigma^2 = E[(n_b^{(r)} - \mu_{re})^2] = E[(n_b^{(i)} - \mu_{im})^2] = \frac{1}{2}E[|n_b - \mu|^2] \tag{3.41}$$

It follows from 3.41

$$\sigma_n^2 = \sigma^2 + \sigma^2 = 2\sigma^2 \tag{3.42}$$

$$\sigma = \frac{1}{\sqrt{2}}\sigma_n. \tag{3.43}$$

From here, we can now define ε as the 99^{th} percentile of the square root of the inverse χ^2 distribution for $2N$ degrees of freedom divided by two, i. e.,

$$\varepsilon = \sqrt{\chi^{-2}(2N)/2}. \tag{3.44}$$

Figure 3.8 demonstrates the difference between the χ^2 distributions for N and $2N$ degrees of freedom and shows that whitened noise on O_{lm} follows a $\chi^2(2N)$ distribution.

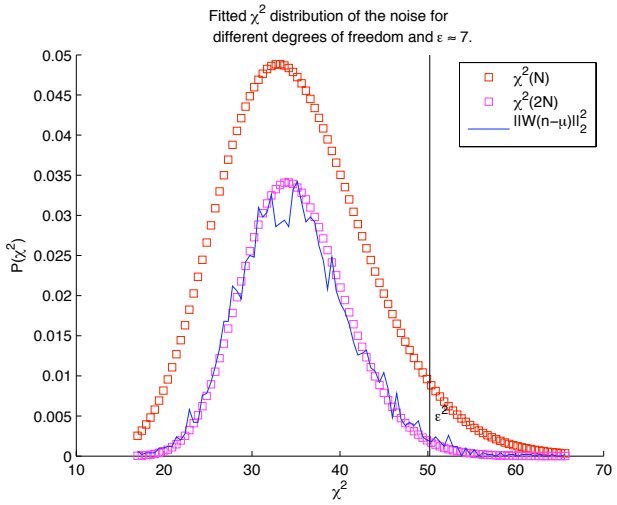

Figure 3.8: χ^2 distributions for N and $2N$ degrees of freedom in comparison with noise distribution on the harmonic coefficients of the ODF (O_{lm}) without signal after whitening and 6000 simulations.

3.3.3 BPDN Problem Formulation with Noise

With the knowledge on the distribution of the noise we are able to set ε to a proper bound. With the residual noise n the whitening operator W from Section 3.3.1 will be applied as follows:

$$o_h = T\bar{o}_h + n \tag{3.45}$$

$$
\begin{aligned}
n &= o_h - T\bar{o}_h && (3.46)\\
\bar{n} &= n - \mu = o_h - \mu - T\bar{o}_h && (3.47)\\
W\bar{n} &= \underbrace{W(o_h - \mu)}_{\check{o}_h} - \underbrace{WT}_{\check{T}}\bar{o}_h. && (3.48)
\end{aligned}
$$

The inverse problem is now redefined with noise and ε as the 99^{th} percentile of the inverse χ^2 distribution for $2N$ degrees of freedom with N being the number of complex unknowns of $\bar{o}_h$, i. e.,

$$
\begin{aligned}
&\text{minimize} && \|\Lambda^{-1}\bar{o}_h\|_1\\
&\text{subject to} && \|\check{o}_h - \check{T}\bar{o}_h\|_2 < \varepsilon
\end{aligned}
\qquad (3.49)
$$

3.4 Extracting Fiber Directions with Maximum Filtering

To evaluate the accuracy of the here proposed sampling and reconstruction techniques, the actual fiber directions need to be extracted. It is generally assumed that the fiber directions are given by the maxima of the ODF or the FOD respectively. For that the method of maximum filtering, as proposed by Lemire [2006] has been used. As we are dealing with a

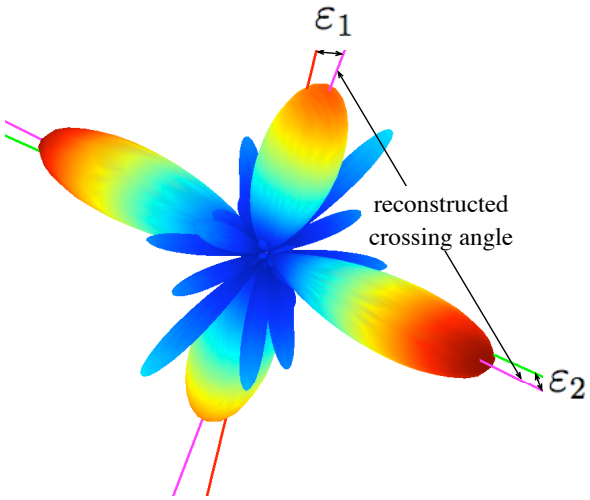

Figure 3.9: Original (red and green) and reconstructed (pink) fiber directions for two crossing fibers. ε_1 and ε_2 represent the reconstruction error for each fiber.

discrete function on a equiangular grid, we can easily extract the maxima. The maximum filtering compares a grid point to its neighbors, which are located within a certain vicinity (window). First, if the value of the observed grid point is higher than its neighbors, it will be selected as a peak candidate by substituting all the neighbors with the value of this peak

candidate. Second, the peaks are found by comparing the modified function with its originate. Hereby, equal entries correspond to maxima of the analyzed function.

The next step is to discard all peaks, which are below 40% of the highest peak, and too far ($\varepsilon_{1,2} \leq 20°$) away from the original fiber, which we aim to reconstruct. This avoids identifying small peaks as fiber directions, which may occur due to noise. Figure 3.9 shows how the reconstruction errors are measured.

"Never postpone until tomorrow what you can do the day after tomorrow."

MARK TWAIN

4 Results

In this chapter we will present the outcome of extensive numerical simulations, which have been conducted to identify the best sampling strategy with respect to fiber extraction from an orientation distribution function (ODF). After choosing the best sampling scheme for the ODF in terms of least possible amount of samples and still reasonable reconstruction quality, we will calculate the fiber orientation distribution (FOD) by means of spherical deconvolution. For FOD calculations we formulate the inverse problem as a basis pursuit denoising (BPDN) problem and apply several modifications to this formulation. Subsequently, we aim in finding the best sampling scheme, which provides best reconstruction quality with respect to the FOD. As a final step we will evaluate our best results in comparison to DSI sampling and reconstruction method.

4.1 Evaluating MWS Sampling Towards a Best Acquisition Strategy with Respect to the ODF

To asses the performance of the proposed sampling and reconstruction technique, simulations have been performed, using a true ODF model as described earlier. We mentioned in Section 3.1 that the novel MWS sampling scheme allows us to estimate the required number of samples for each sampling shell. However, the question on how many shells and to which value of q the shells should be set, cannot be answered with this theorem. Thus, an empirical approach will be evaluated here, in order to find out the best sampling technique. For that, we aim to reconstruct an ODF with two fiber populations from a true ODF with fractional anisotropy of 0.8 and volume fractions of $f_{1,2} = 0.5$. A true ODF will be simulated in 200 random directions and the corresponding signal will be sampled according to a desired sampling scheme. Here, we will investigate the reconstruction quality in terms of sensitivity (i.e., success rate of reconstruction) and accuracy of the result for common diffusion MRI (dMRI) SNR values 20, 30, and 40. As already mentioned earlier in Section 3.4, we set a threshold (40% of the highest peak) on the maxima identification. We discard also results, where the reconstructed fiber directions have an error of more than 20° for each fiber. To measure the accuracy, we will compare the true fiber crossing angle and volume fractions to the reconstructed ones and

propose the best sampling scheme with least possible samples. Here, we exploit the property of the diffusion signal being symmetric. Therefore, we need to sample only one half of the sphere. We will choose from two different distributions of shells, logarithmic and linear. For that, the following settings have been tested as shown in Table 4.1.

Table 4.1: Simulation parameters to evaluate the best sampling scheme.

Shell Placement	**Number of shells**	**Min. b-value** $[sec/mm^2]$	**Max. b-value** $[sec/mm^2]$
logarithmic	2 to 5	0 to 250 (step 50)	2500 to 8000 (step 500)
linear	1 to 5	0 to 250 (step 50)	2500 to 8000 (step 500)

4.1.1 Determination of the Best Sampling Scheme for Fiber Extraction

In this section we will evaluate the performance of fiber reconstruction from the ODF directly by simulating the diffusion weighted MR signal and by applying different sampling strategies. The goal here is to find a sampling where it is possible to reconstruct two crossing fiber populations with an angle of 35° and 40° with the highest sensitivity and with least amount of samples. We chose these angles, because we are not able to resolve fibers crossing with 30°. On the other hand the results for a 45° crossing angle start already to reach sensitivity rates towards 100%. Therefore, the challenging angles for our method are between 35° and 40° fiber crossing angles. Figures 4.1 and 4.2 show the sensitivity plotted for different number of samples for logarithmic and linear distribution of shells and for an SNR = 30. From these extensive simulations, we are now able to conclude on three best sampling settings. In Table 4.2 the sampling parameters, which provide the best reconstruction quality, are shown.

Table 4.2: Best sensitivity results after 200 simulations in random orientations for 35° and 40° crossing angle and SNR = 30.

Shell Placement	**Number of shells**	**Number of samples**	**Sensitivity for 35° [%]**	**Sensitivity for 40° [%]**
linear	1	68	46	73
logarithmic	2	74	43	79
logarithmic	3	79	45	81

It is also worth noting an interesting observation, that using more than one shell for linear placement, does not improve the results. However, when the shells are distributed in a logarithmic fashion, adding more shells provides better reconstruction results for up to three

shells, before the drop in sensitivity rate occurs. This might be explained with the fact, that radial aliasing comes into play with a higher impact for those settings.

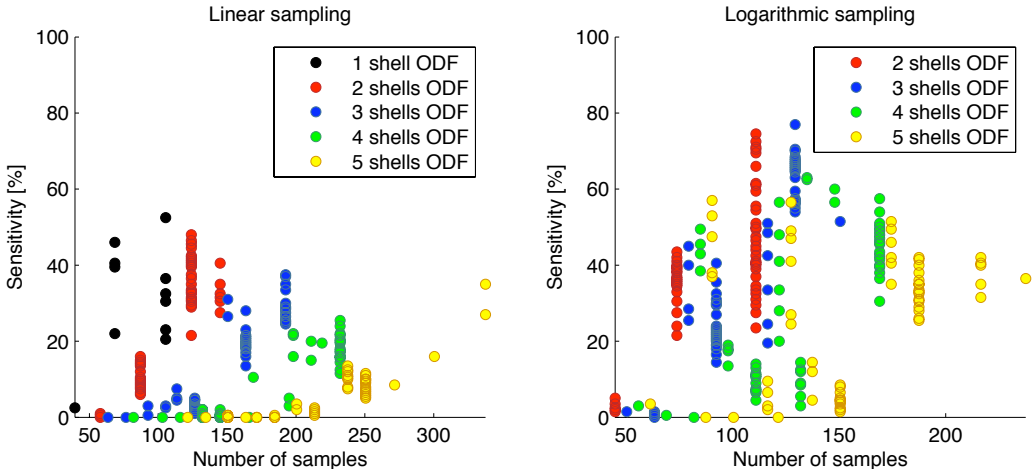

Figure 4.1: Sensitivity rates for different sampling schemes for logarithmic and linear placement of shells, for 35° crossing angle and SNR = 30.

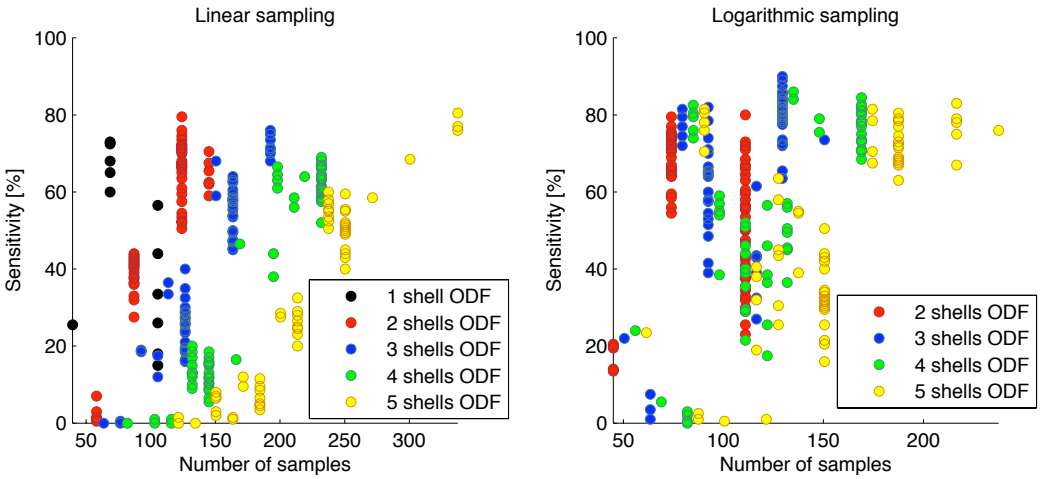

Figure 4.2: Sensitivity rates for different sampling schemes for logarithmic and linear placement of shells, for 40° crossing angle and SNR = 30.

The next step is to run simulations also for the remaining noise levels (SNR = 20 and SNR = 40) and crossing angles, in order to be able to compare the identified schemes among each other. Please refer to Figure 4.3, which shows the outcome of the comparison. Here, we can conclude, that a setting with three logarithmically distributed shells, placed between the b-values of 0 sec/mm^2 and 4000 sec/mm^2, resulting in 79 samples, provides the best results with respect to the ODF. However, we don't know yet which of the three settings will provide best reconstruction results after solving the BPDN problem.

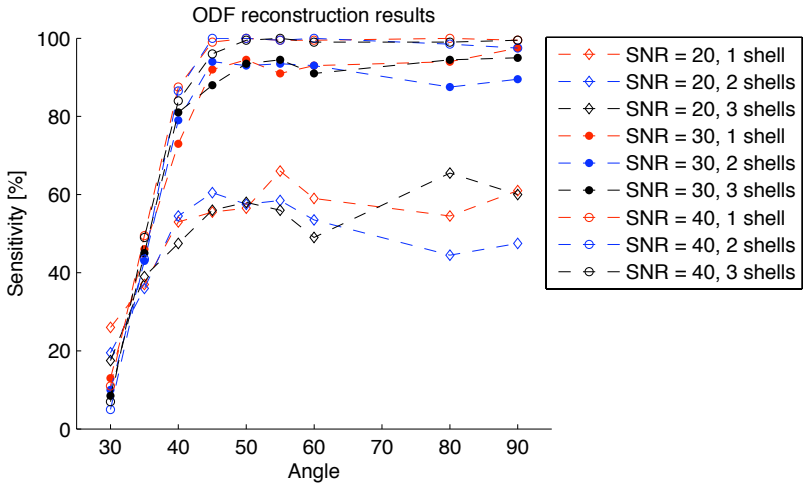

Figure 4.3: ODF sensitivity rates for the three best sampling schemes, for different crossing angles, and SNRs.

4.1.2 Accuracy Evaluation of the Best Sampling Strategy

To also evaluate the accuracy of the best reconstruction scheme (three logarithmic shells, 79 samples, b-values between 0 sec/mm^2 and 4000 sec/mm^2), which we identified in the previous section, we measured the global angular error (Figure 4.4) and the local error $\varepsilon_{1,2}$ (Figure 4.5(a)–(c)) for each fiber. Additionally we also evaluated the error made in reconstruction of the volume fraction of the fibers (Figure 4.5(d)–(f)), where the sum of the lengths of the fibers is 100% and each of the volume fraction contributions should be 50%. For these accuracy evaluations we considered only valid reconstruction results, for each fiber crossing angle. The global angular reconstruction error decreases with increasing SNRs and is around 5°. For the local error $\varepsilon_{1,2}$ we observe the same behavior. Here, it is important to mention, that an error of 5° is small relative to a crossing angle of 90°, however for a crossing angle of 30° means this a relatively high uncertainty. As for the volume fractions, we observe that the reconstruction error also decreases with decreasing noise and stays below 0.05, which corresponds to a relative error of 10%. The boxplots show the error for crossing angles between 30° and 90°, where the central mark is the median, the edges of the box are the 25^{th} and 75^{th} percentiles, the whiskers extend to the most extreme error data points. From visual representation of the ODF for different SNRs in Table 4.3 it can be already concluded that it is not possible to reconstruct a crossing angle of 30°, whereas higher crossing angles $\geq$ 40° can be identified easily. Moreover, we can see that noise introduces many spurious peaks to the ODF or it obstructs the shape of the ODF, such that it is no longer possible to find the fiber directions.

Table 4.3: ODFs for different SNRs and crossing angles. The green and red lines show the true fiber directions and the pink line the reconstructed ones. A sampling scheme with three logarithmic shells and 79 samples was used.

Crossing Angle [°]	True ODF	SNR = 40	SNR = 30	SNR = 20
30		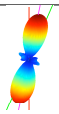	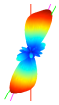	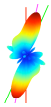
35				
40	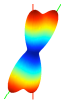	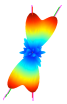	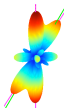	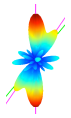
45				

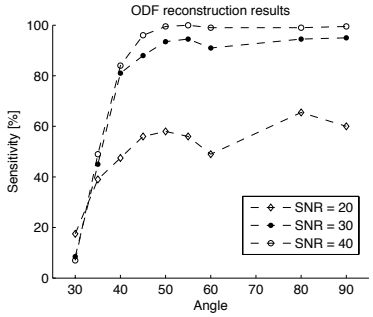

(a) Sensitivity

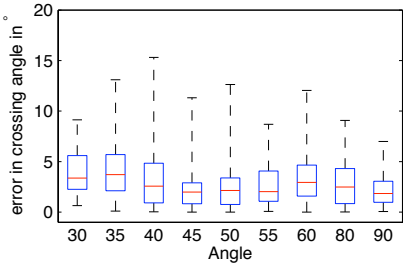

(b) Angular error for SNR = 40

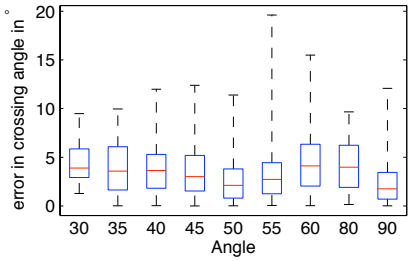

(c) Angular error for SNR = 30

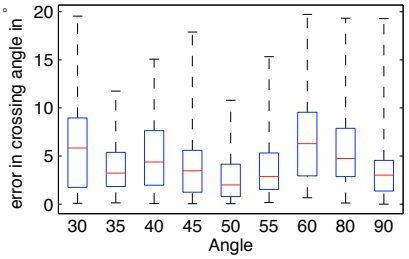

(d) Angular error for SNR = 20

Figure 4.4: Reconstruction accuracy evaluation of the ODF. (a) ODF sensitivity rates for different crossing angles and SNRs for the best sampling scheme with three logarithmic shells and 79 samples. (b)–(d) global angular error.

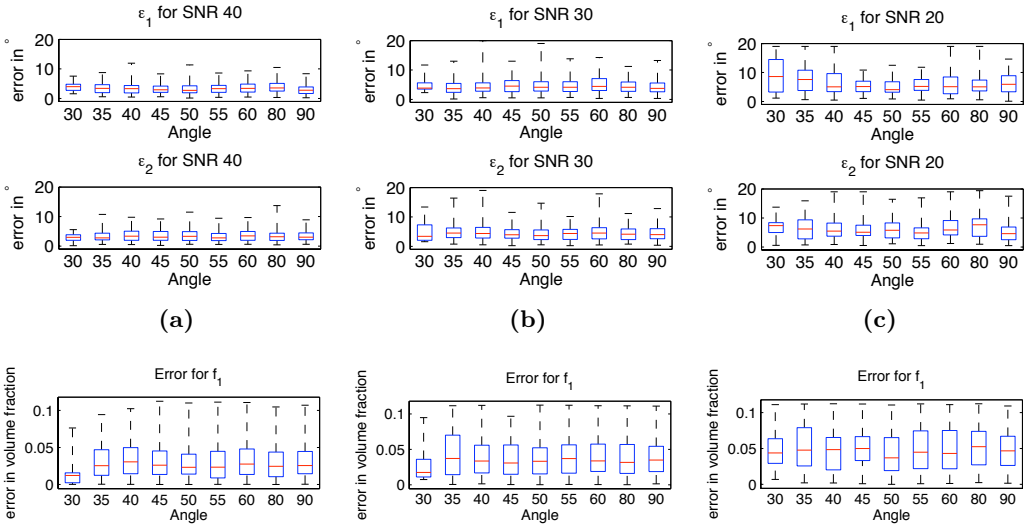

Figure 4.5: Reconstruction accuracy evaluation of the ODF. (a)–(c) angular errors $\varepsilon_{1,2}$ for each of the two reconstructed fibers for different crossing angles and SNRs. (d)–(f) error made in terms of the volume fractions f, where we aimed to reconstruct volume fractions of 0.5 for each of the fiber directions. The sampling scheme with three logarithmic shells and 79 samples was used, which has proven to provide the best results.

4.2 Finding the Best Formulation of the BPDN Problem with Respect to the FOD Using Spherical Deconvolution

We showed that it is possible to obtain already very good results when extracting the fiber directions directly from the ODF. We assume, however, that these results can be improved even further by computing the FOD and again extract the fiber directions from here. In this section we will evaluate the result after solving the BPDN problem. From the computed FOD the fiber directions will be again identified and compared to the results obtained from the ODF. In addition to different sampling schemes, we will also evaluate different formulations of the minimization problem and again compare the results in order to find the best strategy. Therefore, we will use our simulations of the ODF for different crossing angles of two crossing fibers with FA=0.8 and volume fractions $f_{1,2} = 0.5$.

4.2.1 Solving the Inverse Problem for an FOD (BPDN)

Here, we will evaluate the sensitivity rates when calculating the FOD from the ODF by means of our first unmodified version of the BPDN formulation as by Eq. 3.29. From the simulation

results in Figure 4.6 we can see that we cannot improve our results when extracting the fibers from the FOD for SNR=40. However, when comparing the results for a higher noise level (SNR=20), we get an improvement for crossing angles $\geq 50°$.

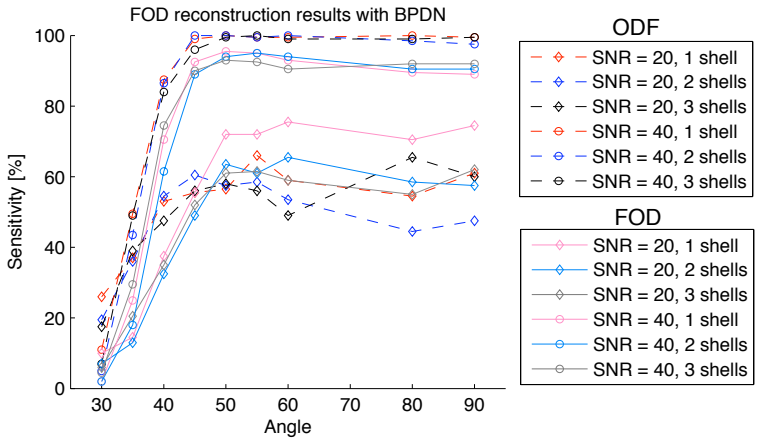

Figure 4.6: FOD reconstruction results (BPDN). Sensitivity rates for three different sampling schemes for different crossing angles and SNRs in comparison to ODF.

Table 4.4: ODFs in comparison to FODs (BPDN) for different SNRs and a 45° crossing angle. The green and red lines show the true fiber directions and the pink line the reconstructed ones. A sampling scheme with one shell has been used.

	SNR		
	40	**20**	**20**
	worst case	**best case**	**worst case**
ODF	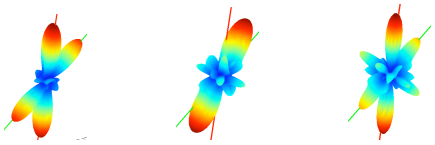		
FOD (BPDN)			

Table 4.4 illustrates worst cases where the FOD distorts the volume fraction of one of the fibers, such that it is no longer recognized as a maximum due to the threshold we set, when extracting the fiber direction. Therefore we hope to solve this problem by modifying the BPDN problem formulation. In best case we manage to resolve 2 fibers with the FOD but not with the ODF even for low SNRs.

4.2.2 Solving the Inverse Problem for an Upsampled FOD (BPDNup)

Earlier, we defined our problem such that we only solve for harmonic coefficients corresponding to even $l > 0$ and $m \geq 0$. As there is no noise on the first harmonic coefficient of the ODF o_0 it cannot be taken into account inside the data constraint. However, the l_1 prior should be able to influence $\bar{o}_0$, as it is part of the solution. In addition to the first harmonic coefficient the sparsity prior can be used to also upsample the result, in order to reduce artifacts caused by the band limit of our function. For that a diagonal matrix D^{down} is used to restrict (downsample) the data constraint to only as many coefficients as provided by the harmonic coefficients of the ODF o_h and excluding the $h = 0$ coefficient. The inverse problem is then reformulated as:

$$\begin{aligned} &\text{minimize} && \|\Lambda^{-1}\bar{o}_h\|_1 \\ &\text{subject to} && \|o_h - TD^{down}\bar{o}_h\|_2 < \varepsilon. \end{aligned} \tag{4.1}$$

Although, the FOD appears to have 'sharper' fibers, we are not able to improve the sensitivity rate with this modification. We observe that the number of reconstructed fibers is altered falsely (see Table 4.5, worst case I). Furthermore, the same effect of distorted fibers as from not upsampled FOD occurs as well when upsampling the FOD (see Table 4.5, worst case II). Therefore, we don't observe any improvement in the sensitivity rates for the fiber reconstructions with this method, as can be seen in Figure 4.7.

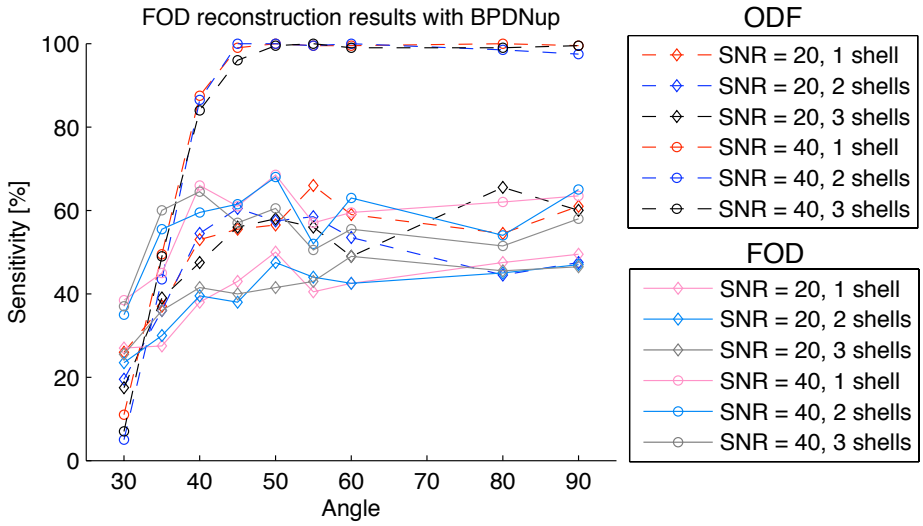

Figure 4.7: FOD reconstruction results (BPDNup). Sensitivity rates for different 3 sampling schemes for different crossing angles and SNRs in comparison to ODF.

Table 4.5: ODFs in comparison with FODs (BPDNup) for SNR=40. The green and red lines show the true fiber directions and the pink line the reconstructed ones. A sampling scheme with three shells has been used. This effect occurs also for one and two shells.

	45° worst case I	45° worst case II	35° best case	80° worst case
ODF	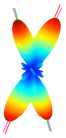		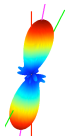	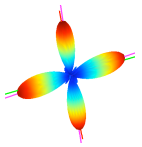
FOD (BPDNup)		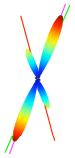		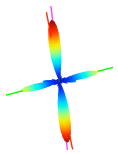

4.2.3 Reformulating the Inverse Problem for FOD in Real Space (BPDNreal)

Another interesting modification to the minimization problem is to solve for the FOD $\bar{o}_h$ already in real space. For that a forward spherical harmonic transform is needed. We denote the forward harmonic transform with a Λ operator and reformulate the inverse problem as:

$$\begin{aligned} &\text{minimize} && \|\bar{O}\|_1 \\ &\text{subject to} && \|o_h - T\Lambda\bar{O}\|_2 < \varepsilon \end{aligned} \tag{4.2}$$

From our simulations we observe a slight improvement in the fiber reconstruction for SNR=40, whereas for SNR=20 and one shell sampling we notice a significant raise of the sensitivity rate for crossing angles $\geq 45°$ (see Figure 4.8).

The last formulation of the problem that we suggest here, is to solve the data constraint completely in real space. Therefore, the ODF O is given and again we are looking for a solution in real space that satisfies the sparsity prior (l_1-norm). In order to be able to perform a convolution with the ODF template T by multiplying the harmonic coefficients of the template with the FOD, we need to make use of the forward and inverse harmonic transform, i.e.,

$$\begin{aligned} &\text{minimize} && \|\bar{O}\|_1 \\ &\text{subject to} && \|O - \Lambda^{-1}T\Lambda\bar{O}\|_2 < \varepsilon \end{aligned} \tag{4.3}$$

Unfortunately, the latter proposal does not allow us to de-correlate the noise in order to be

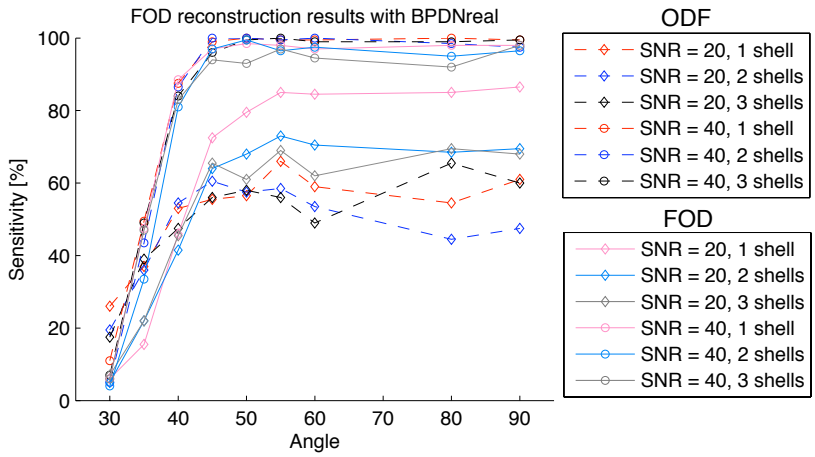

Figure 4.8: FOD reconstruction results (BPDNreal). Sensitivity rates for three different sampling schemes for different crossing angles and SNRs in comparison to ODF.

able to set ε according to the χ^2 distribution. This is the case because the noise on the signal does not only get correlated by linear transformations, but also the inverse spherical harmonic transform creates a linear combination of the harmonic coefficients to obtain the noise on the final ODF O. From here, a whitening operator cannot be created. Therefore, again sufficiently many repetitions (1000) of just noise simulations without signal have been performed. ε was then set to the 99^{th} percentile of the mass of the correlated noise distribution. Unfortunately, with this formulations of the inverse problem it is not possible to improve the reconstruction results, due to inaccurate estimation of ε.

A disadvantage of the real space formulation of the minimization is that it does not make sense to upsample the result. As our signal is bandlimited, the forward harmonic transform would create aliasing and distort the result.

Table 4.6: ODFs in comparison with FODs from different BPDN problem formulations. The green and red lines show the true fiber directions and the pink line the reconstructed ones. We can see that with BPDN in real space (BPDNreal) we manage to reconstruct two fibers, without distorting the volume fractions.

	True ODF	**ODF**	**FOD BPDNup**	**FOD BPDNreal**
SNR 40, 3 shells, 45°	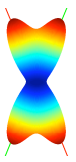	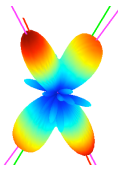	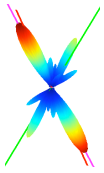	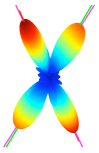

From Table 4.6 we can see that the volume fractions and the number of fibers can be reconstructed more accurately, when we solve for an ODF in real space instead of for its harmonic coefficients.

4.2.4 Adding a Positivity Constraint to the Inverse Problem (BPDNreal+)

As reported by Tournier [2007] spherical deconvolution introduces negative spurious peaks to the FOD producing a physically impossible solution. Therefore, the inverse problem will be constrained to positive values of the ODF only, because it is known that the ODF as well as the FOD are not only symmetric but also positive functions. We therefore reformulate the inverse problem as:

$$\begin{aligned} \text{minimize} \quad & \|\bar{O}\|_1 \\ \text{subject to} \quad & \|o_h - T\Lambda\bar{O}\|_2 < \varepsilon, \\ & \bar{O} > 0, \end{aligned} \tag{4.4}$$

with $\bar{O} > 0$ being the positivity constraint. Adding the positivity constraint improves the results only for one case of the proposed formulations of the BPDN problem, namely for solving the problem for an ODF in real space (BPDNreal). The reconstruction results of the ODF calculated by other formulations could not be improved.

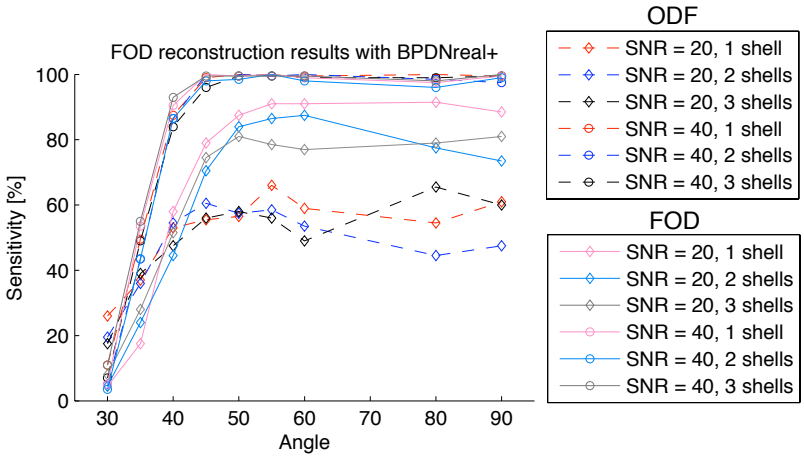

Figure 4.9: FOD reconstruction results (BPDNreal+). Sensitivity rates for three different sampling schemes for different crossing angles and SNRs in comparison to ODF.

Figure 4.9 shows that we can reach angular resolutions up to 45° for high noise levels (SNR = 20) and even up to 40° for lower noise levels (SNR = 40), when using the BPDNreal+ formulation.

We can conclude from this result, that we are able to denoise the FOD very well by using the BPDN formulation of the inverse problem. In addition, we can note that by calculating the FOD we can even have very good results with only 68 samples on one shell, which is not possible for the fiber reconstruction from an ODF. At this step we identified the best combination of a sampling scheme with one shell and 68 samples and a modified version of the BPDN formulation (BPDNreal+).

4.2.5 Accuracy Evaluation with Respect to FOD (BPDNreal+)

From our simulations we can see that the BPDN problem formulation for an FOD in real space (BPDNreal+) in combination with a single shell sampling scheme with 68 samples has proven to be the best strategy. In this section we will show the accuracy we can reach with this sampling and reconstruction technique. Again, we evaluate only the valid results, according to the sensitivity rates. From the Figures 4.10 and 4.11 we observe that the local angular error $\varepsilon_{1,2}$ is improved, when we reconstruct the fibers from the FOD. However, there is a small deterioration in the global angular error, although the error mean remains around 5°. The volume fractions are not influenced by the transformation to the FOD.

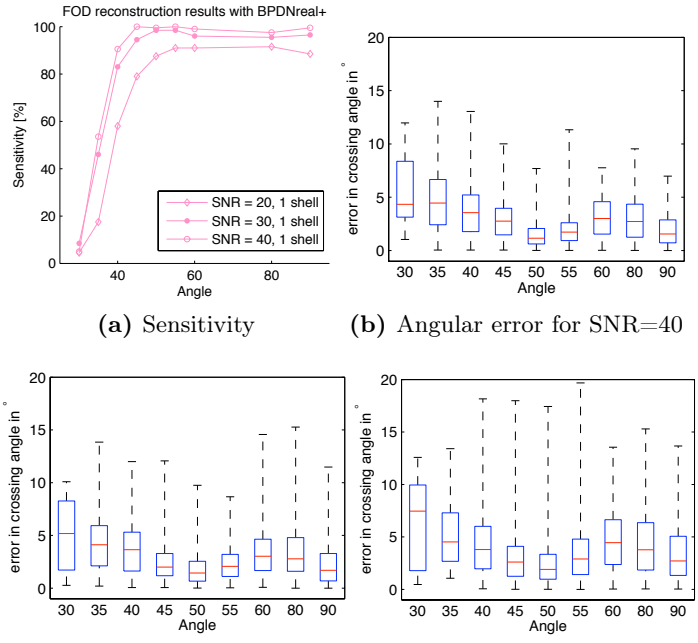

(a) Sensitivity **(b)** Angular error for SNR=40

(c) Angular error for SNR=30 **(d)** Angular error for SNR=20

Figure 4.10: Reconstruction accuracy evaluation of the FOD (BPDNreal+). (a) sensitivity rates for different crossing angles and SNRs. (b)–(d) global angular error. Sampling scheme with one logarithmic shell and 68 samples

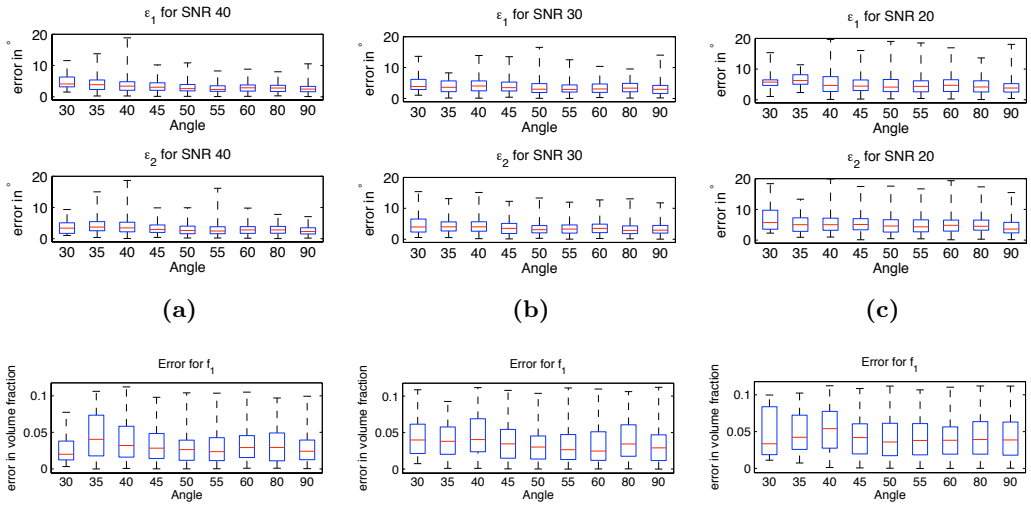

(a) **(b)** **(c)**

(d) f-error for SNR=40 **(e)** f-error for SNR=30 **(f)** f-error for SNR=20

Figure 4.11: Reconstruction error for ε and volume fractions from the FOD (BPDNreal+). (a)–(c) angular errors $\varepsilon_{1,2}$ for each of the two reconstructed fibers for different crossing angles and SNRs. (d)–(f) error made in terms of the volume fractions f, where we aimed to reconstruct volume fractions of 0.5 for each of the fiber directions. Sampling scheme with one shell and 68 samples

4.3 Comparison: FOD (BPDNreal+), ODF, and DSI

In the previous section we identified the best sampling scheme and the best formulation of the minimization problem to calculate the FOD, which leads us to the next question: How is the performance of our approach in comparison with DSI? We conducted numerical simulations for DSI with b-values up to $8000 sec/mm^2$ and for different SNR values. Figure 4.12 shows the sensitivity rates for all three methods, which are: ODF from DSI sampling, ODF and FOD with MWSS and BPDNreal+.

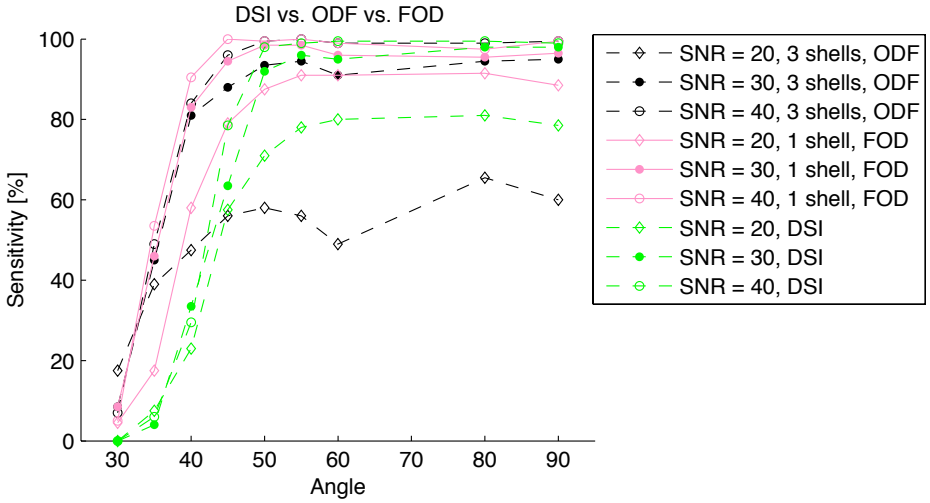

Figure 4.12: Sensitivity rates of the best sampling schemes with respect to ODF and FOD (BPDNreal+) for different crossing angles and SNRs in comparison with DSI.

With the new sampling scheme we are able to reach higher angular resolutions than with DSI sampling method. For DSI the symmetry can be also exploited, thus making it possible to reduce the amount of samples for DSI by a factor of two. However, even with this modification, the new sampling method requires only 79 samples on three shells, which is less than 258 needed for DSI. When reconstructing the fiber directions from the ODF, we are able to resolve crossings of 40° in comparison to 50° with DSI. If we calculate the FOD we are even able to outperform the reconstruction rates of the ODF with even less samples (68) and only one shell. This reconstruction technique allows us to further improve the sensitivity rate by approximately 30% for high noise levels (SNR = 20) and by 5% for low noise levels (SNR = 40).

"There are no facts, only interpretations"

FRIEDRICH NIETZSCHE

5 Discussion

In this thesis we have developed a novel fiber reconstruction method for diffusion magnetic resonance imaging (dMRI) measurements based on spherical sampling and spherical deconvolution. Many methods for fiber reconstruction exist and the use of spherical harmonics to approximate a signal in q-space became a common approach in dMRI. However, up to now, none of the methods tackled the problem of radial aliasing, which arises when a signal is sampled with an improper bandwidth.

Here, we evaluated a novel sampling theorem on the sphere [McEwen and Wiaux, in press] (MWS), which allowed us to probe at low band-limit (B<11) diffusion signals with less than half the number of samples as required by other equiangular sampling theorems on the sphere [Driscoll and Healy, 1994]. Although, the MWS sampling theorem provides us with constraints on the number of samples for each shell (i.e., to avoid angular aliasing), the information on where (i.e., which b-values) to place the shells in q-space is unknown. The extensive numerical simulations, provided in this thesis, identified the best sampling strategy for fiber reconstruction from an orientation distribution function (ODF). Hereby, a sampling scheme with 79 q-space samples placed on three logarithmically distributed shells has proven to be the best signal acquisition strategy. To our surprise, adding more sampling shells does not necessary lead to better reconstruction results. Especially, using linear placement of shells, the reconstruction became even worse by increasing the amount of shells. However, when simultaneously increasing the b-value, we could observe a general improvement in reconstruction performance. This effect remains an open question, but we speculate that high radial aliasing has an impact when the signal is sampled in an improper way in radial direction. Together, we conclude that with fiber reconstruction from the ODF, logarithmic spherical sampling provides higher sensitivity rates than linear sampling.

Furthermore, we proposed spherical deconvolution as a technique to further increase angular resolution between crossing fibers. Spherical deconvolution is applied to the ODF in order to calculate the fiber orientation distribution (FOD), which provides better reconstruction results than the ODF. This complex operation can be performed efficiently in harmonic space since it is being reduced to an inverse problem and can be reformulated as a basis pursuit denoising problem (BPDN). BPDN is known to be able to suppress noise and at the same

time preserve well-expressed structures of the solution. Solving the inverse problem for an FOD in harmonic space is computationally advantageous due to small number of unknowns to be determined. Unfortunately, when looking for a band-limited function in harmonic space, aliasing artifacts are being introduced when transforming the solution back to real space. Therefore, we proposed to solve the BPDN problem for an upsampled FOD and exploit the nice feature of harmonic transformation allowing us to increase the band-limit. As expected, after upsampling the aliasing artifacts disappeared, however, the overall sensitivity couldn't be improved. The reason for this behaviour was mainly caused by distorted volume fractions of the FOD, which lead to non-optimal maxima extraction. To address this issue, we proposed to solve the inverse problem for an FOD in real space, as we assume that the problem of incorrectly reconstructed volume fractions is caused by fitting the harmonic coefficients instead of solving for the FOD function itself. Indeed, we observed an improvement in comparison to the upsampled FOD solution in terms of fiber reconstruction sensitivity. The final modification of the BPDN problem aimed to remove negative values of the FOD in real space, which are physically not possible. These negative values occur due to noise. By constraining the FOD to only positive values we were finally able to outperform the reconstruction results of the ODF, especially in the range of high noise levels (SNR = 20).

Summarized, this led us to the conclusion that a constrained BPDN formulation of the inverse problem, together with a sampling scheme with 68 samples on one shell, is the best approach to reconstruct fiber crossings. This is not only an improvement in terms of angular resolution but also in terms of number of samples. Finally, we compared our results to the model-free diffusion spectrum imaging (DSI) reconstruction method. This comparison revealed a clear advantage for our method in terms of number of samples and, more importantly, angular resolution between two crossing fibers.

Although, many ideas towards improving the extraction of the fiber directions from diffusion weighted data have been investigated, some approaches still remained untouched during this work. One interesting idea is to test the reconstruction performance of the FOD calculated by the original formulation of the BPDN problem [Chen et al., 1995]:

$$\begin{aligned} &\text{minimize} && \|\bar{O}\|_1 \\ &\text{subject to} && \|O - \Phi\bar{O}\|_2 < \varepsilon. \end{aligned} \tag{5.1}$$

The BPDN problem is solved in real space with an overcomplete dictionary Φ containing a one-fiber ODF template, also referred to as atoms, rotated in all possible directions. Then we aim to find the best solution of the linear combinations of the atoms to model the sampled ODF. For example to model an ODF, which represents two fibers crossing in one voxel, a linear combination of two one-fiber templates will be found to conclude on the FOD.

Another formalism to solve the inverse problem has caught our attention as well. Due to difficulties we have experienced, when dealing with noise, least absolute shrinkage and selection operator (LASSO) method may be a better alternative to solve the inverse problem. This algorithm was suggested by Tibshirani [1994] and minimizes the residual (l_2-norm) subject to the sum of the coefficients (l_1-norm) being less than a constant κ (see Eq. 5.2). In our case κ represent the maximum number of fibers we aim to reconstruct.

$$\begin{aligned} &\text{minimize} && \|E - \Phi\bar{O}\|_2 \\ &\text{subject to} && \|\bar{O}\|_1 \leq \kappa \end{aligned} \tag{5.2}$$

When using LASSO, we don't need to set ε anymore, thus having more freedom in reformulating the inverse problem. Now a totally different approach may be used, where the FOD is obtained from the signal E directly. And with the LASSO formulation of the inverse problem in real space we don't need to make use of the spherical harmonics. Additionally, as we don't go to harmonic space, we don't have to worry about aliasing errors making the use of the sampling theorem obsolete. These modification would allow us to experiment with different sampling grids and numbers of samples to finally identify an optimal sampling and fiber reconstruction strategy.

Here, I would also like to mention one disadvantage of the spherical deconvolution technique. We need to make assumptions on the fractional anisotropy (FA) of the one-fiber template. For all of our simulations we have set the FA of the true ODF as well as of the ODF template to 0.8. It will certainly influence the reconstruction quality of the FOD if the fractional anisotropy measures do not match, which would be interesting to observe and to evaluate. On the other hand we are able to reconstruct as many fibers as we want, as long we can resolve the angle between the fibers (see Figure 5.1).

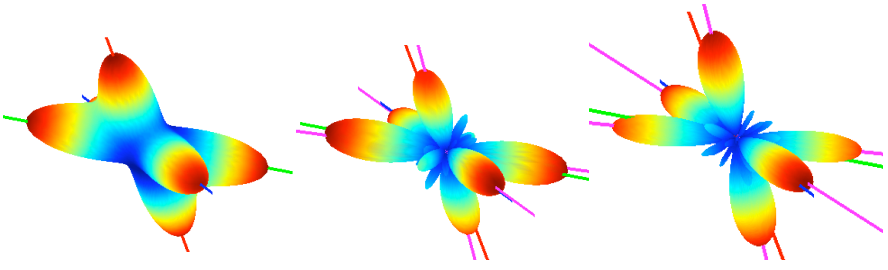

(a) True ODF **(b)** ODF **(c)** FOD (BPDNreal+)

Figure 5.1: Three fibers crossing in one voxel. A noise of SNR=40 was applied to the diffusion signal. The true ODF (a), the reconstructed ODF (b), and the FOD using BPDNreal+ (c) are shown. A sampling scheme with 68 samples on one shell has been applied.

The influence of compressed sensing (i.e., undersampling) on further reduction of samples leading to reduced sampling time should also be exploited. Undersampling of diffusion-weighted MR images in k-space can be considered in this context, but also reducing the number of samples on each shell in q-space is an option. In combination, this would have an influence on the acquisition time. However, it is of course not clear whether a reasonable reconstruction quality can be achieved.

Real data acquisition is another topic, which could not be touched due to time reasons, but is crucial to make the evaluation of the method complete. For that purpose and in order to make conclusions on the reconstruction quality a phantom may be used, where the crossing angle of the fibers is known.

Taken together, we showed that resolving neuronal pathways with the help of spherical harmonics and techniques used in compressed sensing leads to a better reconstruction quality than popular reconstruction methods such as DSI.

"The truth is our most precious possession, thus let us be economical in its use."

MARK TWAIN

6 Conclusion

In this thesis work we have evaluated a novel sampling theorem on the sphere within the context of diffusion MRI and we also presented a new fiber orientation distribution reconstruction technique. The novelty in the reconstruction approach is the use of the knowledge from the field of compressed sensing and the application of basis pursuit denoising to the spherical deconvolution technique. After extensive numerical simulations, we showed that this strategy made it possible to reliably estimate fiber direction with a lower angle than with an orientation distribution function. In comparison to diffusion spectrum imaging, we were be able to reach a relatively high angular resolution of 40° crossing fibers with only 68 samples, instead of 50° with 258 samples. The improvement of the fiber orientation reconstruction quality with our method may lead to development of robust and more accurate tractography algorithms, paving the way for further interesting clinical research studies and possibly even applications.

Bibliography

I. Aganj, C. Lenglet, and G. Sapiro. ODF reconstruction in q-ball imaging with solid angle consideration. *Biomedical Imaging: From Nano to Macro, 2009. ISBI'09. IEEE International Symposium on*, pages 1398–1401, 2009.

I. Aganj, C. Lenglet, G. Sapiro, E. Yacoub, K. Ugurbil, and N. Harel. Reconstruction of the orientation distribution function in single- and multiple-shell q-ball imaging within constant solid angle. *Magnetic Resonance in Medicine*, 64(2):554–566, 2010.

H. E. Assemlal, D. Tschumperlé, L. Brun, and K. Siddiqi. Recent advances in diffusion mri modeling: Angular and radial reconstruction. *Medical Image Analysis*, In Press, Corrected Proof:–, 2011.

P. J. Basser, J. Mattiello, and D. LeBihan. MR diffusion tensor spectroscopy and imaging. *Biophysical journal*, Jan 1994.

C. Beaulieu. The basis of anisotropic water diffusion in the nervous system–a technical review. *NMR in Biomedicine*, Jan 2002.

F. Bloch. Nuclear Induction. *Physical Review Online Archive (Prola)*, 70(7-8):460–474, October 1946.

E. Canales-Rodriguez. Mathematical description of q-space in spherical coordinates: Exact q-ball imaging. *Magnetic Resonance in Medicine*, Jan 2009.

H. Y. Carr and E. M. Purcell. Effects of diffusion on free precession in nuclear magnetic resonance experiments. *Phys. Rev.*, 94(3):630–638, May 1954.

S. S. Chen, D. Donoho, and M. A. Saunders. *Basis Pursuit*. PhD thesis, Standford University, November 1995.

K. H. Cho, C. H. Yeh, J. D. Tournier, Y. P. Chao, J. H. Chen, and C. P. Lin. Evaluation of the accuracy and angular resolution of q-ball imaging. *Neuroimage*, 42(1):262–271+, 2008.

A. Daducci, J. D. McEwen, D. Van De Ville, J. P. Thiran, and Y. Wiaux. Harmonic analysis of spherical sampling in diffusion MRI. In *International Soc. for Magn. Reson. Med. (ISMRM) conference*, page 3929, 2011.

M. Descoteaux. *High Angular Resolution Diffusion MRI: From Local Estimation to Segmentation and Tractography*. PhD thesis, Universite de Nice - Sophia Antipolis, Febuary 2008.

J. R. Driscoll and D. M. Healy. Computing fourier transforms and convolutions on the 2-sphere. *Advances in Applied Mathematics*, 15(2):202 – 250, 1994.

D. Fuhrmann. *Complex Random Variables and Stochastic Processes*, chapter 60. CRC Press LLC, 1999. ISBN 978-1-4200-4604-5.

P. Hagmann, L. Cammoun, X. Gigandet, R. Meuli, C. J. Honey, and O. Sporns. Mapping the Structural Core of Human Cerebral Cortex. *PLOS Biology*, 6(7):e159, 2008.

P. Hagmann, L. Jonasson, P. Maeder, J. P. Thiran, V. J. Wedeen, and R. Meuli. Understanding Diffusion MR Imaging Techniques: From Scalar Diffusion-weighted Imaging to Diffusion Tensor Imaging and Beyond. *Radiographics*, 26(suppl 1):S205–S223, October 2006.

E. L. Hahn. Spin echoes. *Phys. Rev.*, 80(4):580–594, Nov 1950.

H. Johansen-Berg and T.E.J. Behrens. *Diffusion MRI: from quantitative measurement to in-vivo neuroanatomy*. Academic Press. Elsevier/Academic Press, 2009. ISBN 9780123747099.

D. K. Jones and P. J. Basser. "Squashing peanuts and smashing pumpkins": how noise distorts diffusion-weighted MR data. In *Magn. Reson. Med. 52*, pages 979–993, 2004.

D. M. Koh and D. J. Collins. Diffusion-Weighted MRI in the Body: Applications and Challenges in Oncology. *Am. J. Roentgenol.*, 188(6):1622–1635, June 2007.

D. LeBihan. Looking into the functional architecture of the brain with diffusion MRI. *Nature Reviews Neuroscience*, 4(6):469–480, 06 2003.

D. LeBihan, E. Breton, D. Lallemand, P. Grenier, E. Cabanis, and M. Laval-Jeantet. MR imaging of intravoxel incoherent motions: application to diffusion and perfusion in neurologic disorders. *Radiology*, 161(2):401–407, November 1986.

D. Lemire. Streaming maximum-minimum filter using no more than three comparisons per element. *Nordic Journal of Computing*, 13(4):328–339, 2006.

Yoshitaka Masutani, Shigeki Aoki, Osamu Abe, Naoto Hayashi, and Kuni Otomo. MR diffusion tensor imaging: recent advance and new techniques for diffusion tensor visualization. *European Journal of Radiology*, 46(1):53 – 66, 2003.

J. D. McEwen and Y. Wiaux. A novel sampling theorem on the sphere. *IEEE Transactions on Signal Processing*, in press.

S. Mori and J. Zhang. Principles of diffusion tensor imaging and its applications to basic neuroscience research. *Neuron*, 51(5):527 – 539, 2006.

M. E. Moseley, Y. Cohen, J. Mintorovitch, L. Chileuitt, H. Shimizu, J. Kucharczyk, M. F. Wendland, and P. R. Weinstein. Early detection of regional cerebral ischemia in cats: comparison of diffusion- and T2-weighted MRI and spectroscopy. *Magnetic resonance in medicine*, 14(2):330–346, May 1990.

S. Pajevic and C. Pierpaoli. Color schemes to represent the orientation of anisotropic tissues from diffusion tensor data: Application to white matter fiber tract mapping in the human brain. *Magnetic Resonance in Medicine*, 42(3):526–540, 1999.

E. M. Purcell, H. C. Torrey, and R. V. Pound. Resonance Absorption by Nuclear Magnetic Moments in a Solid. *Physical Review Online Archive (Prola)*, 69(1-2):37–38, January 1946.

V. J. Schmithorst and W. Yuan. White matter development during adolescence as shown by diffusion MRI. *Brain and Cognition*, 72(1):16 – 25, 2010. Adolescent Brain Development: Current Themes and Future Directions.

E. O. Stejskal and J. E. Tanner. Spin diffusion measurements: Spin echoes in the presence of a time-dependent field gradient. *The Journal of Chemical Physics*, 42(1):288–292, 1965.

D. G. Taylor and M. C. Bushell. The spatial mapping of translational diffusion coefficients by the NMR imaging technique. *Physics in Medicine and Biology*, 30(4):345–349, 1985.

R. Tibshirani. Regression Shrinkage and Selection Via the Lasso. *Journal of the Royal Statistical Society, Series B*, 58:267–288, 1994.

J. Tournier. Robust determination of the fibre orientation distribution in diffusion MRI: non-negativity constrained super-resolved spherical deconvolution. *NeuroImage*, Jan 2007.

J. Tournier, F. Calamante, D. Gadian, and A. Connelly. Direct estimation of the fiber orientation density function from diffusion-weighted MRI data using spherical deconvolution. *NeuroImage*, 23(3):1176–1185, November 2004.

J.D. Tournier, S. Mori, and A. Leemans. Diffusion tensor imaging and beyond. *Magnetic Resonance in Medicine*, 65(6):1532–1556, 2011.

D. Tuch. Q-ball imaging. *Magnetic Resonance in Medicine*, 52(6):1358–1372, December 2004.

D. Tuch. *Diffusion MRI of Complex Tissue Structure*. PhD thesis, Harvard University and Massachusetts Institute of Technology, January 2002.

V. J. Wedeen. Mapping fiber orientation spectra in cerebral white matter with Fourier transform diffusion MRI. In *In Proc. of the 8th Annual Meeting of ISMRM*, page 82, 2000.

V. J. Wedeen, R. P. Wang, J. D. Schmahmann, T. Benner, W.Y.I. Tseng, G. Dai, D.N. Pandya, P. Hagmann, H. D'Arceuil, and A.J. de Crespigny. Diffusion spectrum magnetic resonance imaging (DSI) tractography of crossing fibers. *NeuroImage*, 41(4):1267 – 1277, 2008.

G. E. Wesbey, M. E. Moselet, and R. L. Ehman. Translational Molecular Self-Diffusion in Magnetic Resonance Imaging: II. Measurement of the Self-Diffusion Coefficient. *Investigative Radiology*, 19(6), 1984.

C. F. Westin and S. E. Maier. A Dual Tensor Basis Solution to the Stejskal-Tanner Equations for DT-MRI. *International Society for Magnetic Resonance in Medicine*, 10:1–1, May 2002.

T. H. Williams, N. Gluhbegovic, and J. Y. Jew. Virtual Hospital: The Human Brain: Dissections of the Real Brain, 1997.

List of Figures

List of Tables

A Appendix

A.1 Solving the Gaussian Integral

$$
\begin{aligned}
\int e^{-1/2\mathbf{r}^T D_i^{-1}\mathbf{r}} r^2 dr &= I_n(a) \\
I_n(a) &= \int e^{-ax^2} x^n dx \\
x &\equiv a^{-1/2} y \\
dx &= a^{-1/2} dy \\
y^2 &= ax^2 \\
I_n(a) &= a^{-1/2} \int e^{-y^2} (a^{-1/2} y)^n dy \\
&= a^{-(n+1)/2} \int e^{-y^2} y^n dy
\end{aligned}
$$

For $n = 0$, this is just the usual Gaussian integral,

$$
I_0(a) = \frac{1}{2}\sqrt{\frac{\pi}{a}}
$$

For $n = 1$, the integrand is integrable by quadrature

$$
\begin{aligned}
I_1(n) &= a^{-1} \int e^{-y^2} y dy = a^{-1} \left[-\frac{1}{2} e^{-y^2} \right]_0^\infty = \frac{1}{2a} \\
-\frac{\partial}{\partial a} I_{n-2}(a) &= -\frac{\partial}{\partial a} \int e^{-ax^2} x^{n-2} dx \\
&= -\int -x^2 e^{-ax^2} x^{n-2} dx \\
&= \int -ax^2 x^n dx \\
&= I_n(a)
\end{aligned}
$$

for even n

$$\begin{aligned} I_n(a) &= -\frac{\partial}{\partial a} I_{n-2}(a) \\ &= \left(-\frac{\partial}{\partial a}\right)^2 I_{n-4} \\ &= \cdots = \left(-\frac{\partial}{\partial a}\right)^{n/2} I_0(a) \\ &= \frac{\sqrt{\pi}}{2}\left(-\frac{\partial}{\partial a}\right)^{n/2} a^{-1/2} \\ \int x^2 e^{-ax^2} dx &= \frac{\sqrt{\pi}}{4a^{3/2}} \end{aligned} \tag{A.1}$$